DEFECTS IN PERSISTENT LUMINESCENCE MATERIALS

by

Taneli Laamanen

Laboratory of Materials Chemistry and Chemical Analysis
Department of Chemistry
University of Turku
FI-20014 Turku
FINLAND

and

Graduate School of Materials Research
Turku
FINLAND

Supervised by

Professor Jorma Hölsä and Docent Mika Lastusaari
Laboratory of Materials Chemistry and Chemical Analysis
Department of Chemistry
University of Turku
FI-20014 Turku
FINLAND

Reviewed by

Professor Dirk Poelman
LumiLab
Department of Solid State Sciences
Ghent University
Krijgslaan 281 / S1
B-9000 Gent
BELGIUM

and

Doctor Karel Knížek
Institute of Physics ASCR
Department 24
Cukrovarnicka 10
CZ-16200 Prague 6
CZECH REPUBLIC

Opponent

Professor Marco Bettinelli
Laboratory of Solid State Chemistry
Department of Biotechnology
University of Verona and INSTM
UdR Verona
Strada Le Grazie 15
IT-37134 Verona
ITALY

PREFACE

Turku, August 2011

Taneli Laamanen

ABSTRACT

Persistent luminescence materials can store energy from solar radiation or artificial lighting and release it over a period of several hours without a continuous excitation source. These materials are widely used to improve human safety in emergency and traffic signalization. They can also be utilized in novel applications including solar cells, medical diagnostics, radiation detectors and structural damage sensors. The development of these materials is currently based on methods based on trial and error. The tailoring of new materials is also hindered by the lack of knowledge on the role of their intrinsic and extrinsic lattice defects in the appropriate mechanisms. The goal of this work was to clarify the persistent luminescence mechanisms by combining *ab initio* density functional theory (DFT) calculations with selected experimental methods. The DFT approach enables a full control of both the nature of the defects and their locations in the host lattice. The materials studied in the present work, the distrontium magnesium disilicate ($Sr_2MgSi_2O_7$) and strontium aluminate ($SrAl_2O_4$) are among the most efficient persistent luminescence hosts when doped with divalent europium Eu^{2+} and co-doped with trivalent rare earth ions R^{3+} (R: Y, La-Nd, Sm, Gd-Lu).

The polycrystalline materials were prepared with the solid state method and their structural and phase purity was confirmed by X-ray powder diffraction. Their local crystal structure was studied by high-resolution transmission electron microscopy. The crystal and electronic structure of the non-doped as well as Eu^{2+}, $R^{2+/3+}$ and other defect containing materials were studied using DFT calculations. The experimental trap depths were obtained using thermoluminescence (TL) spectroscopy. The emission and excitation of $Sr_2MgSi_2O_7$:Eu^{2+},Dy^{3+} were also studied.

Significant modifications in the local crystal structure due to the Eu^{2+} ion and lattice defects were found by the experimental and DFT methods. The charge compensation effects induced by the R^{3+} co-doping further increased the number of defects and distortions in the host lattice. As for the electronic structure of $Sr_2MgSi_2O_7$ and $SrAl_2O_4$, the experimental band gap energy of the host materials was well reproduced by the calculations. The DFT calculated Eu^{2+} and $R^{2+/3+}$ $4f^n$ as well as $4f^{n-1}5d^1$ ground states in the $Sr_2MgSi_2O_7$ band structure provide an independent verification for an empirical model which is constructed using rather sparse experimental data for the R^{3+} and especially the R^{2+} ions. The intrinsic and defect induced electron traps were found to act together as energy storage sites contributing to the materials' efficient persistent luminescence. The calculated trap energy range agreed with the trap structure of $Sr_2MgSi_2O_7$ obtained using TL measurements. More experimental studies should be carried out for $SrAl_2O_4$ to compare with the DFT calculations. The calculated and experimental results show that the electron traps created by both the rare earth ions and vacancies are modified due to the defect aggregation and charge compensation effects. The relationships between this modification and the energy storage properties of the solid state materials are discussed.

Keywords: strontium magnesium disilicate, strontium aluminate, europium, rare earth, lattice defect, persistent luminescence, density functional theory calculations

TABLE OF CONTENTS

SYMBOLS AND ABBREVIATIONS

a	Unit cell parameter / Å
A_B	Atom A in atom B site
A_i	Interstitial atom A
APW	Augmented plane wave
ASW	Augmented spherical wave
b	Unit cell parameter / Å
B3LYP	Becke three-parameter Lee-Yang-Parr functional
B3PW	Becke three-parameter Perdew-Wang functional
BLYP	Becke-Lee-Yang-Parr functional
BP	Becke-Perdew functional
c	Unit cell parameter / Å
CB	Conduction band
CT	Charge transfer
EPR	Electron paramagnetic resonance
F, F^+	Color centre
DFPT	Density functional perturbation theory
DFT	Density functional theory
DFTB	Density functional based tight binding approach
DOS	Density of states
$Dy_{Sr}^{\bullet}$	Trivalent dysprosium in Sr^{2+} site, single positive net charge
EECE	Exact exchange of correlated electrons
E	Energy / eV
E_g	Energy of band gap / eV
Eu_{Sr}^{x}	Divalent europium in Sr^{2+} site, zero net charge
em	Emission
exc	Excitation
GGA	Generalized gradient approximation
h^+	Hole
HF	Hartree-Fock method
H_{KS}	Kohn-Sham Hamiltonian
I	Intensity
INS	Inelastic neutron scattering
IR	Infrared
J	Magnetic coupling constant, exchange parameter / eV
LAPW	Linearized augmented plane wave
LCAO	Linear combination of atomic orbitals
L(S)DA	Local (spin) density approximation
LMTO	Linear muffin-tin orbital
n/a	Not available
no.	Number
OSL	Optically stimulated luminescence
$O_i^{''}$	Interstitial oxygen, double negative net charge

PAW	Projector augmented wave
PP	Pseudopotential
R	Rare earth
Ref.	Reference
RT	Room temperature
R_{Sr}^{x}	Divalent rare earth in Sr^{2+} site, zero net charge
$R_{Sr}^{\bullet}$	Trivalent rare earth in Sr^{2+} site, single positive net charge
SR	Synchrotron radiation
T_s	Kinetic energy of the non-interacting particles / eV
TD-DFT	Time-dependent density functional theory
TEM	Transmission electron microscopy
TL	Thermoluminescence
TSL	Thermally stimulated luminescence
U	Coulomb repulsion strength, Hubbard parameter / eV
UV	Ultraviolet
V	Potential energy / eV
VB	Valence band
vis	Visible
VUV	Vacuum ultraviolet
V_A	A atom vacancy
V_{Al}'''	Aluminium vacancy, triple negative net charge
V_{Mg}''	Magnesium vacancy, double negative net charge
$V_{O}^{\bullet\bullet}$	Oxygen vacancy, double positive net charge
V_{Si}''''	Silicon vacancy, quadruple negative net charge
V_{Sr}''	Strontium vacancy, double negative net charge
XPD	X-ray powder diffraction
Z	Number of formula units per unit cell
Z	Point at the Brillouin zone boundary
β	Lattice parameter / Degrees
Γ	Origin of the Brillouin zone
ε_i	Energy of single particle / eV
λ	Wavelength / nm
μ_{xc}	Local exchange-correlation energy density function
ρ	Ground state electron density
φ_i	Mathematical single particle wave function
∇^2	Laplace operator

1. INTRODUCTION

A luminescent material emits electromagnetic radiation usually in the visible range, though emission of ultraviolet (UV) or infrared (IR) radiation may also be observed [1]. Luminescence is due to excitation of the system to a higher energy state characteristic to the material. This is followed by a radiative transition to a lower state. The luminescent solid materials (phosphors) usually consist of an inorganic host material which is activated by introducing *e.g.* rare earth ions as dopants in the host lattice [2]. The rare earths (R) include the elements from La (Z: 57) to Lu (71) which are also called lanthanides as well as the elements Sc (21) and Y (39). The efficient shielding of the $4f^n$ (n: 1-14) electrons by the $5s^2$ and $5p^6$ electrons results in similar chemical properties of the lanthanides with a few exceptions. They show characteristic intraconfigurational 4f luminescence which is almost independent of the selected host lattice since their absorption and emission energies are only weakly affected by the external electric fields. The lanthanide ions are usually employed in the trivalent form as activators in the luminescent materials; however the divalent Sm^{2+}, Yb^{2+} and – most notably – Eu^{2+} ions are commonly used activators, as well.

High purity of the conventional phosphors is required since the luminescent efficiency of the rare earth ions is usually drastically lowered when impurities and defects are present in the host lattice [3]. However, the excitation energy may be stored in the material with the introduction of lattice defects which can act as energy storing traps. The energy storage is exploited by two main applications: optically stimulated luminescence (OSL) and thermally stimulated luminescence (TSL) or, more commonly, photostimulated and persistent luminescence materials, respectively.

The persistent luminescence phenomenon commences with the storage of the excitation energy from natural or artificial lighting which is followed by its gradual release induced by the thermal energy available at a specific – usually room – temperature (RT). Long-lasting continuous luminescence can thus be obtained after the removal of the excitation source. Persistent luminescence is an unwanted afterglow phenomenon in phosphors used as *e.g.* scintillators and in the plasma display panels. However, the persistent luminescence materials are widely used in *e.g.* self-lit signalization and they can also be applied to fluorescent tubes for emergency lighting. These materials show potential in radiation detection [4] and medical diagnostics [5], as well.

The most efficient persistent luminescent materials include the alkaline earth aluminates and magnesium disilicates doped with Eu^{2+} and co-doped with other rare earth ions, $CaAl_2O_4$:Eu^{2+},Nd^{3+} [6], $SrAl_2O_4$:Eu^{2+},Dy^{3+} [6-8], $Sr_4Al_{14}O_{25}$:Eu^{2+},Dy^{3+} [9] and $Sr_2MgSi_2O_7$:Eu^{2+},Dy^{3+} [10-12]. The best materials emit in visible even in excess of 24 h in the dark. The luminescence properties of the aluminates (especially MAl_2O_4) degrade when exposed to water and hence their replacement with the more stable disilicate based materials as *e.g.* pigments in luminous paints has been considered.

Several persistent luminescence mechanisms describing the energy storage and release processes have been suggested. However, the earliest ones were deficient in many ways since they failed to correctly account for the energetics, kinetics and the role of the lattice defects [*e.g.* 6,8,11]. In addition, they could not explain the persistent luminescence observed from the Eu^{2+} doped materials without the R^{3+} co-doping [13]. The most recent mechanisms [14] account for all of the

details mentioned above, though the exact role of the co-doping R^{3+} ions as well as that of the other defects remains uncertain.

The energy storage properties are simultaneously affected by several energy level systems: the structure of the valence (VB) and conduction band (CB) including the energy gap between them, the $4f^n$ ground and $4f^{n-1}5d^1$ state energies of the R^{2+} and R^{3+} ions – including the Eu^{2+} luminescent centre – as well as the energies of the other lattice defects. The systematic tailoring of the defect chemistry to obtain the desired energy storage and emission properties will only be possible when the details of the different energy schemes as well as the interplay between them are known.

The $R^{2+/3+}$ $4f^n$ and $4f^{n-1}5d^1$ ground state energies in the host's band structure can be estimated using an empirical model [e.g. 14-17]. However, this model is constructed using experimental spectroscopic data usually consisting of wide bands and thus the exact energies are difficult to obtain. In addition, experimental data does not exist for all R^{3+} ions and it exists only for a very few R^{2+}. Finally, this model does not take into account e.g. the charge compensation induced by the doping or electronic relaxation effects. Theoretical calculations and their comparison with the experimental results are thus an attractive alternative to solve the exact $R^{2+/3+}$ energies since their experimental confirmation is very difficult or impossible.

The intrinsic defects in the $Sr_2MgSi_2O_7$ and $SrAl_2O_4$ persistent luminescence host materials include e.g. the strontium ($V_{Sr}^{''}$ with a double negative net charge as indicated by the Kröger-Vink notation) and oxygen vacancies ($V_O^{\bullet\bullet}$ with a double positive net charge) as well as the interstitials and dislocations (Fig. 1). $V_{Sr}^{''}$ and $V_O^{\bullet\bullet}$ can be created due to the evaporation of SrO during the high temperature solid state reaction frequently necessary for the enhanced performance of the material. Cation vacancies also exist in the materials as a result of charge compensation when the R^{3+} ion replaces the Sr^{2+} host cation ($R_{Sr}^{\bullet}$). Oxygen vacancies may be created in the lattice due to the reducing preparation conditions, as well. A high number of the energy storing traps which can be bleached in the ambient conditions is required to obtain the long duration of the persistent luminescence. Defect aggregates are also expected to exist in the materials since the aggregation probability should increase with increasing defect concentration.
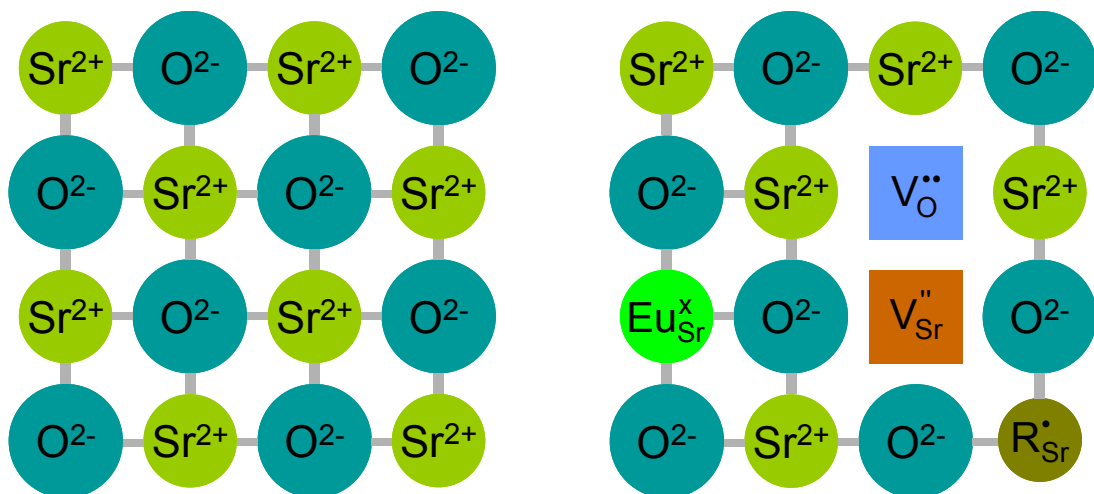
Figure 1. Pure (left) and lattice defect containing ($V_{Sr}^{''}$: double negative, $V_O^{\bullet\bullet}$: double positive, $R_{Sr}^{\bullet}$: single positive, Eu_{Sr}^{x}: zero net charge, right) SrO sublattice.

The goal of this work was to clarify the mechanism of the persistent luminescence by employing a systematic approach combining *ab initio* density functional theory (DFT) calculations with the appropriate experimental methods. The DFT calculations allow the control of both the nature of the defects and their locations in the host lattice which cannot be probed experimentally. The crystal and electronic structure of the non-doped $Sr_2MgSi_2O_7$ and $SrAl_2O_4$ host materials as well as their modification with the introduction of the Eu^{2+} luminescent centre, $R^{2+/3+}$ ions and other lattice defects were studied. The role of the defects and defect aggregates as possible electron or hole trapping sites which may contribute to the energy storage efficiency of the materials was studied, too.

The distrontium magnesium disilicates doped with Eu^{2+} and co-doped with Dy^{3+} ($Sr_2MgSi_2O_7$:Eu^{2+},Dy^{3+}) were prepared with a solid state reaction. The microscopic and even nanoscale structure of the materials was studied with high-resolution transmission electron microscopy (TEM) to determine the influence of the lattice defects on the local structure.

Simultaneously, the DFT calculations were carried out in order to reveal first the structure of the valence and conduction bands as well as the band gap energy of $Sr_2MgSi_2O_7$ and $SrAl_2O_4$. Then, the modification of the crystal structure as well as the energies of the isolated defect (Eu_{Sr}^x, R_{Sr}^x, $R_{Sr}^\bullet$, V_{Sr}'', V_{Si}'''', V_{Mg}'', and $V_O^{\bullet\bullet}$) and defect aggregate ($Eu_{Sr}^x + V_{Sr}''$, $Eu_{Sr}^x + V_O^{\bullet\bullet}$ and $V_{Sr}'' + V_O^{\bullet\bullet}$) states in the $Sr_2MgSi_2O_7$ band structure were calculated. The isolated defects (Eu_{Sr}^x, V_{Sr}'', V_{Al}''' and $V_O^{\bullet\bullet}$) were studied also in $SrAl_2O_4$. The $4f^n$ and $4f^{n-1}5d^1$ ground state energies of all the divalent (R^{2+}, R: La-Lu) and trivalent (R^{3+}) lanthanide ions in $Sr_2MgSi_2O_7$ were studied, as well.

Eventually, the trap energy structure and luminescence properties of the $Sr_2MgSi_2O_7$:Eu^{2+}(,Dy^{3+}) materials were studied using the thermoluminescence (TL) and synchrotron radiation luminescence spectroscopy, respectively. The relationships between the experimental and calculated trap energy structure and the luminescence properties of the materials were determined. The energy transfer and storage processes occurring in the persistent luminescence materials are discussed based on the combined theoretical and experimental results.

Most of the work included in this thesis has been presented in the following publications referred to as I-VII in the text.

I.   Furusho, H., Hölsä, J., Laamanen, T., Lastusaari, M., Niittykoski, J., Okajima, Y., and Yamamoto, A., Probing Lattice Defects in $Sr_2MgSi_2O_7$:Eu^{2+},Dy^{3+}, *J. Lumin.* **128** (2008) 881-884.

II. Hölsä, J., Laamanen, T., Lastusaari, M., Niittykoski, J., and Novák, P., Electronic Structure of the $SrAl_2O_4$:Eu^{2+} Persistent Luminescence Material, *J. Rare Earths* **27** (2009) 550-554.

III. Hölsä, J., Kirm, M., Laamanen, T., Lastusaari, M., Niittykoski, J., and Novák, P., Electronic Structure of the $Sr_2MgSi_2O_7$:Eu^{2+} Persistent Luminescence Material, *J. Lumin.* **129** (2009) 1560-1563.

IV. Hölsä, J., Laamanen, T., Lastusaari, M., and Novák, P., Structure Optimization and Electronic Structure of the $SrAl_2O_4$:Eu^{2+} Persistent Luminescence Material by DFT Calculations, *Terrae Rarae 2009* (2010) 13/1-6.

V.   Hassinen, J., Hölsä, J., Laamanen, T., Lastusaari, M., and Novák, P., Electronic Structure of Defects in $Sr_2MgSi_2O_7$:Eu^{2+},La^{3+} Persistent Luminescence Material, *J. Non-Cryst. Solids* **356** (2010) 2015-2019.

VI. Furusho, H., Hassinen, J., Hölsä, J., Laamanen, T., Lastusaari, M., Niittykoski, J., and Yamamoto, A., Influence of Defects on the Luminescence Properties of the $Sr_2MgSi_2O_7$:Eu^{2+},Dy^{3+} Persistent Luminescence Material, manuscript.

VII. Hölsä, J., Laamanen, T., Lastusaari, M., and Novák, P., A DFT Study on the Defects and Defect Aggregates in $Sr_2MgSi_2O_7$, manuscript.

2. DENSITY FUNCTIONAL THEORY CALCULATIONS OF SOLID MATERIALS

2.1. Density Functional Theory

A solid state material can be described as a many body system consisting of electromagnetically interacting electrons and nuclei. Though direct solution of this kind of quantum many body problem is not possible, the problem can be accurately addressed when the necessary approximations are applied. As a starting point, the Born-Oppenheimer approximation [18] is used to place the nuclei at fixed positions since their movement is vanishingly slow when compared with the movement of the much lighter electrons. The quantum many body problem is thus reduced to a system of interacting electrons moving in the potential of the nuclei at fixed positions. This problem can be treated rather well with the Hartree-Fock method (HF) [19-21] for atoms and molecules; however, this method does not treat the solid state materials with sufficient accuracy.

The density functional theory is presently the most powerful tool for the calculation of the properties of solid materials. In addition, the DFT method is not limited by the Born-Oppenheimer approximation and can thus be used to describe solids with light elements which move significantly faster than the heavy ones. The DFT method is based on the theorems of Hohenberg and Kohn which state that the total energy of a system (E_{tot}) of interacting electrons in the external potential of the nuclei is given exactly as a functional of the ground state electron density (Eq. 1) [22,23]:

$$E_{tot} = E_{tot}(\rho_\uparrow, \rho_\downarrow) \tag{1}$$

where $\rho_\uparrow$ and $\rho_\downarrow$ are the spin up and down ground state electron densities, respectively. The theorems show that the density which minimizes $E_{tot}(\rho_\uparrow, \rho_\downarrow)$ is the true ground state electron density. Furthermore, all observable ground state quantities of the material are functionals of the ground state density. Therefore, the ground state electron density contains as much information of the material as the wave function does. The unknown energy functional $E_{tot}(\rho_\uparrow, \rho_\downarrow)$ can be rewritten in order to obtain the ground state density (Eq. 2) [24]:

$$E_{tot}(\rho_\uparrow, \rho_\downarrow) = T_s(\rho_\uparrow, \rho_\downarrow) + E_{ee}(\rho_\uparrow, \rho_\downarrow) + E_{Ne}(\rho_\uparrow, \rho_\downarrow) + E_{xc}(\rho_\uparrow, \rho_\downarrow) + E_{NN} \tag{2}$$

where the electronic contributions are the kinetic energy of the non-interacting particles (T_s), the electron-electron Coulomb repulsion (E_{ee}), nuclear-electron attraction (E_{Ne}), and exchange-correlation energies (E_{xc}). E_{NN} is the repulsive energy of the fixed nuclei. The form of the exchange-correlation functional has to be determined before the ground state electron density can be calculated. The most widely used approximation method is the local (spin) density approximation (L(S)DA) for the non-spin-polarized (spin-polarized) systems where the exchange-correlation functional has the following form (Eq. 3) [24]:

$$E_{xc} = \int \mu_{xc}(\rho_\uparrow, \rho_\downarrow)[\rho_\uparrow + \rho_\downarrow] dr \tag{3}$$

In this expression, μ_{xc} is the local exchange-correlation energy density function. In the LDA method, the material is divided into very small volumes with constant density and the exchange-correlation of each volume is assumed to be equal to the known exchange-correlation energy of an identical volume filled with a homogeneous electron gas. The LDA method has been refined by the generalized gradient approximation (GGA) method which replaces $\mu_{xc}\left(\rho_\uparrow, \rho_\downarrow\right)$ with a local function of the density and the magnitude of its gradient. Therefore, several forms of μ_{xc} exist for the GGA method [e.g. 25-28].

The most recent improvements in the DFT methods include the hybrid methods, *e.g.* the exact exchange for correlated electrons (EECE) method [29]. In this method, the exchange (and correlation) between correlated and uncorrelated orbitals are treated using LDA or GGA since they are expected to describe such interactions accurately. Only the exchange within the correlated subshell on each atom is treated by the exact Hartree-Fock expression in the EECE method. Currently used hybrid functionals include *e.g.* B3PW [30], B3LYP [31] and Fock-α [32].

Using the corresponding Kohn-Sham Hamiltonian obtained from Eq. 2, a set of single particle Schrödinger type equations known as Kohn-Sham equations [33] can be written (Eq. 4):

$$\left[-\nabla^2 + V_{Ne} + V_{ee} + V_{xc}\right]\varphi_i(r) = \varepsilon_i\varphi_i(r) \tag{4}$$

where φ_i are the wave functions (orbitals) of mathematical single particles at the point r and ε_i are the single particle energies (eigenvalues). The combined density of these single particles is equal to the true electron density, though the individual particles do not have a physical meaning [33].

The advantage of the DFT approach is that only a series of single particle equations has to be solved instead of solving an immensely difficult many body Schrödinger equation [24]. However, a selfconsistent procedure is required to calculate the Kohn-Sham orbitals since both the Hartree potential (V_{ee}) and the exchange-correlation potential (V_{xc}) depend on the electron density. Therefore, an iterative calculation process has to be employed (Fig. 2). In this process, a starting electron density is estimated to construct the Kohn-Sham Hamiltonian (H_{KS}). A series of single particle Kohn-Sham equations is solved to find out the single particle orbitals which are used to derive the output electron density. This density is used as an input for the next iteration and the process is repeated until a consistent ground state electron density is found.

2.2. Calculation Methods

Several calculation methods exist to solve the Kohn-Sham equations for obtaining the ground state electron density, total energy, and energy bands (eigenvalues) of a solid state material. The simplest approaches include the single particle and molecular calculation methods. However, the calculation of the solid state materials requires a more sophisticated approach. The cluster model [34,35] is a step forward from the molecular calculations. In this model, a finite cluster consisting of different regions is used to represent a crystal lattice. The inner region consists of a quantum mechanically treated cluster centered on the defect site which is surrounded by interface ions and a region of classical shell model ions, whereas the outer region consists of point charges.

guess $\rho_0(r)$

input: $\rho_{n-1}(r)$

determine V_H and V_{xc}

H_{KSn}

solve $H_{KSn}\,\varepsilon_n = \varepsilon_n\,\phi_n$

ϕ_n

construct ρ_n from ϕ_n

$\rho_n = \rho_{n-1}$?

no

yes

ρ_n is selfconsistent density
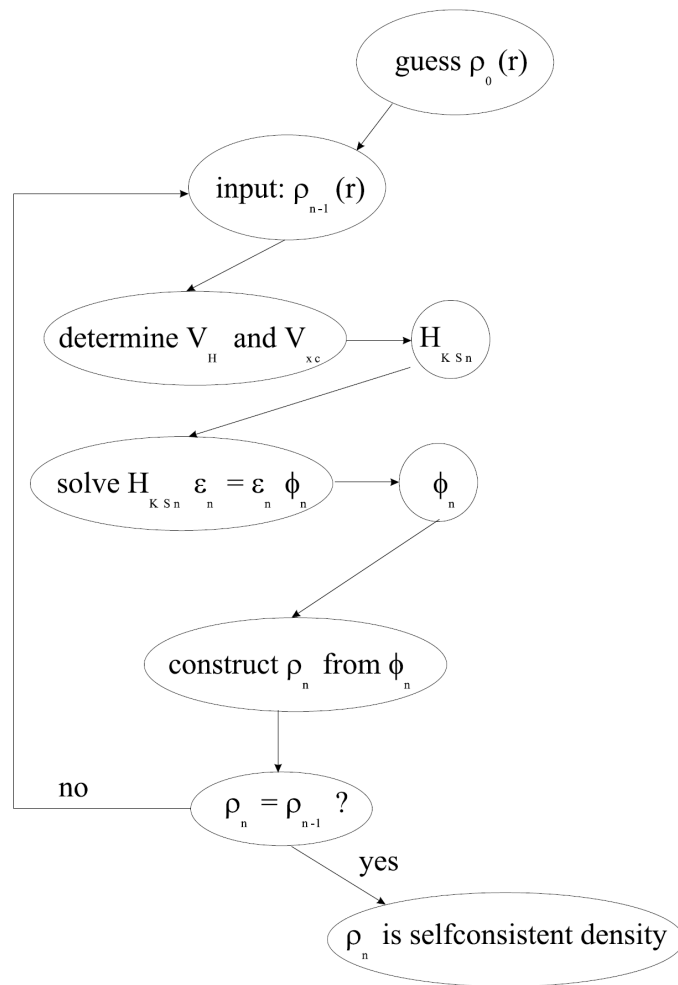
Figure 2. Flow chart of the selfconsistent procedure to calculate the ground state electron density using the Kohn-Sham equations [36].

The current DFT calculation methods rely on a basis set expansion of the single particle Kohn-Sham orbitals. Expansion coefficients are used to express the orbitals in a given basis set [24]. Therefore, the choice of the basis set reduces the solution of the selfconsistent Kohn-Sham equations to the determination of the expansion coefficients for the orbitals which minimize the total energy. Relatively simple plane wave basis sets have been traditionally used in the pseudopotential (PP) method. However, the conventional plane wave basis set is not an ideal choice for the solution of the Schrödinger's equation in a crystal lattice since the potential and therefore the wavefunctions change rapidly near the nuclei. This problem has been addressed in the pseudopotential method by replacing the Hamiltonian near the atoms with a smoother pseudo-Hamiltonian. A more complex but efficient basis set is employed by the linearized muffin-tin orbital (LMTO) and linearized augmented plane wave (LAPW) methods. In the LAPW method, the plane waves near the atoms are modified instead of the Hamiltonian.

The LAPW method is based on the augmented plane wave method (APW) [37,38] which is currently not in active use mainly due to its computationally demanding calculation procedure. In the more efficient LAPW method, the crystal lattice is divided into non-overlapping atomic spheres and the interstitial region. The orbitals are described by spherical harmonics in the atomic spheres which

are centered at the atomic sites. The electron states are divided into the core and valence states. The core states are contained in the atomic spheres, whereas the valence states are expanded by using the basis functions. These functions have the form of a plane wave in the interstitial region and each one is augmented by an atomic type function in every atomic sphere. Local orbitals are added to the basis functions to increase the flexibility of the basis as well as to enable the treatment of two valence functions with the same orbital number (*e.g.* the 3p and 4p functions). The LAPW method allows the use of a much smaller basis set than the one constructed from regular plane waves alone. The size of the basis set can be further decreased by increasing the radius of the atomic spheres, though this decreases the accuracy of the calculations [24].

2.3. Applications

The elastic and thermodynamic properties of the solid state materials can be studied by the DFT calculations (Table 1) [39-44]. The density functional perturbation theory (DFPT) [45] enables the calculation of lattice dynamics and response to external electromagnetic fields. The phonon frequencies and dispersion curves including the Raman as well as inelastic neutron scattering (INS) spectra and the electron-phonon interactions can be calculated using the DFPT method [46-51]. The electronic host band structure which includes the structure of the valence and conduction bands as well as the band gap energy can be obtained from the calculated ground state electron density [50,52-57]. The DFT method provides a very important means to probe the magnetic properties including the exchange interaction [58-60], magnetic moment [29,61,62], hyperfine field [63-65], Kerr spectrum [66-68] and Jahn-Teller distortion [69], as well.

The DFT calculations can be used to study the optical properties of the solid state materials, as well (Table 1) [46,70-85]. The optical absorption can be obtained from the dielectric function which describes the linear response of an insulator to an applied electric field [70]. The imaginary part of the dielectric tensor is directly related to the electronic band structure of a solid and can thus be calculated from the single particle orbitals and energies. The real part can then be obtained since the real and imaginary parts are linked by a Kramers-Kronig transformation.

Excitation energy calculations using the time dependent density functional theory (TD-DFT) method have been successfully applied for molecular systems (Table 1) [*e.g.* 71-73]. This method can also describe the optical transitions of surface and bulk lattice defects in simple solids as *e.g.* MgO [83,85] and Al_2O_3 [81]. However, the direct calculation of the selected transitions is not possible using the TD-DFT method as a large number of states with very low transition probabilities has to be included in the calculations [74]. Therefore, the calculation of the excitation energies in the solid state materials with more complicated crystal structures is very difficult.

The rare earth ion containing materials provide a difficult challenge for the DFT calculations due to the strong correlation of their 4f electrons. The ionization potentials [86-88] as well as the bond energies [89,90] of the rare earth atoms and molecules can be calculated using the simple one-particle, molecular and cluster model DFT calculation methods (Table 2). However, *e.g.* the pseudopotential, LAPW or LMTO methods (*cf.* section 2.2.) have to be employed for the calculation of the solid state materials where the host lattice consists partly of the rare earth ions. The total

energy [91,92], host band structure [70,93-103] and magnetic properties [104,105] of these materials have been calculated.

Table 1. DFT studies of inorganic solid state materials.

	Calculated property	Material	DFT calculation method	Exchange-correlation method	Ref.
Elastic and thermodynamic properties	Bulk modulus, entropy, heat capacity	$Na_2Ti_3O_7$	PP	LDA	39
		AlN	PP	GGA	40
		M_2B (M: Cr-Ni, Mo, W)	PP	GGA	41
		NiO	LMTO	LDA+U	42
		BaX (X: S, Se, Te)	PP	LDA	43
		Bi	DFPT, PP	LDA	44
Lattice dynamics	Phonon band structure	NH_4F, $NaHF_2$, SiO_2	DFPT, PP	LDA, GGA	46,47
		Al, Pb nanowire, Bi	DFPT, PP	LDA	48,49
		$Ca_2MgSi_2O_7$	DFPT, PP	LDA	50
		Pb_2MgTeO_6	DFPT, PP	LDA	51
Electronic	Electronic band structure	Li_2SiO_3, $Li_2Si_2O_5$	PAW	GGA	52
		$MgTi_2O_4$	PP	B3LYP	53
		$Ca_2MgSi_2O_7$	DFPT, PP	LDA	50
		NiO	LMTO	LDA+U	54
		$SrAl_2O_4$	PP	GGA	55
		$(ZrO_2)_x(SiO_2)_{1-x}$	PP	LDA	56
		$PbSiO_3$	PP	LDA, GGA	57
Magnetic	Exchange interaction	MnO, $BaFe_{12}O_{19}$, $Ba_{2-x}Sr_xZn_2Fe_{12}O_{22}$	LAPW	LDA, GGA, GGA+U	58-60
	Magnetic moment	MO (M: Mn-Ni), Fe_3O_4, FeF_2, FeAl, Gd	LAPW	LDA, LDA+U, GGA, EECE, B3PW, B3LYP, Fock-α	29,61, 62
	Hyperfine field	Li_3N:Fe, Fe, Fe_3O_4, FeF_3, Fe:R (R: La-Lu), Fe:An (An: Ac-Lr), Co, Ni	LAPW	LDA, LDA+U, B3PW	63-65
	Kerr spectrum	CrO_2, Fe, Fe_3O_4, Co, Ni	LAPW	LDA, LDA+U, GGA	66-68
	Jahn-Teller distortion	$LaMnO_3$	PP, LAPW	LDA, LDA+U, GGA	69
Optical	IR absorption	SiO_2	PP	GGA	46
	VUV-vis absorption	$CaGeO_3$	PP	LDA, GGA	75
		$SrB_2Si_2O_8$	PP	LDA	76
		$CdSiO_3$	PP	LDA, GGA	77
		$BiVO_4$	PP	GGA	78
	X-ray absorption	SiO_2, Cu, La_2CuO_4	PP, PAW	GGA	79
		$(YM)_2BaNiO_5$	LAPW	LDA, LDA+U, GGA	80
	Excited states of point defects	MgO, MgO:Na, Al_2O_3, SiO_2, SiO_2:Ge	TD-DFT, cluster	LDA, GGA, B3LYP	81-85

Table 2. DFT studies of rare earth containing materials.

	Calculated property	Material	Rare earth	DFT calculation method	Exchange-correlation method	Ref.
Atoms and molecules	Ionization potential	R atom	La-Lu	One-particle	LDA, GGA	86
		RX_3 (X: F, Cl, Br, I)	La, Gd, Lu	Molecular	LDA, GGA, BLYP	87
		RS	La, Ce, Eu, Gd, Yb, Lu	Molecular	GGA	88
	Bond energy	RO, YbF	La, Eu, Gd, Yb	Molecular	GGA	89
		RF, YbH	Nd, Eu, Gd, Yb	Cluster	BP, BLYP, B3LYP	90
Solid state materials	Total energy	Eu metal, EuO, EuS, EuSe, EuTe	Eu	LAPW	LDA+U	91
		R_2O_3	La-Lu	PP	GGA, B3PW, B3LYP	92
	Host band structure	R metal	Sm-Gd	PP	GGA	93
		$NaRP_2O_7$, $NaR(PO_3)_4$, $KR(PO_3)_4$	Ce, Eu	PP	GGA	94,95
		RN	La-Lu	LMTO	LDA+U	96
		PrO_2, $BaPrO_3$	Pr	LAPW	LDA+U	97
		R_2O_2Te	La, Sm, Gd	PP	GGA	98
		RF_3	Ce, Tb	LAPW, LMTO	GGA, LDA+U	99,100
		RSF	La, Ce	LAPW	GGA	70
		RAs, YAs	Er-Lu	LMTO	LDA	101
		$R_3Co_4Sn_{13}$	La, Ce, Sm, Gd, Tb	LAPW	GGA	102
		CeRhZn	Ce	ASW	LDA	103
		$LuAlO_3$:Ce^{3+}	Ce, Lu	LMTO	LDA	100
	Magnetic moment	RCr_2Si_2	Tb, Er	LAPW	GGA	104
		PrZnPO	Pr	LAPW, LMTO	LDA+U, EECE	105

Only few studies exist on the DFT calculation of the electronic structure of the rare earth doped solid state materials. Prior to this work, no reports existed on the *ab initio* calculation of the $4f^n$ or the $4f^{n-1}5d^1$ ground state energies for the $R^{2+/3+}$ series in any solid state host. The pseudopotential method has been used for the calculation of the energies of some isolated R^{3+} ions (R: Sm, Eu, Er, Tm) as well as R^{3+} containing defect aggregates in the electronic band structure of some simple host materials (Table 3) [106-114]. The formation and binding energies of defect aggregates have been studied using DFT, as well [106-109,111,113,114]. The structural modifications in the host

induced by the rare earth doping have been studied by the optimization of the crystal structure with the DFT calculations [106,109-114].

Table 3. DFT studies of the electronic structure of rare earth doped solid state materials.

Material	Defect	DFT calculation method	Exchange-correlation method	Ref.
$AlN:R^{3+}$ (R: Eu, Er, Tm)	R_{Al}, $R_{Al}+O_N$, $R_{Al}+(O_N)_2$, $R_{Al}+V_N$	PP	LDA	106
$Si:Er^{3+}$	$Er_i+(O_i)_n$ (n: 1-6)	PP	LDA	107,108
$SiC:Er^{3+}$	Er_{Si}, $Er_{Si}+N_C$, $Er_{Si}+H_i$	PP	LDA	109
$TiO_2:Sm^{3+}$	Sm_{Ti}	PP	GGA	110
$GaN:R^{3+}$ (R: Eu, Er, Tm)	R_{Ga}, R_i, N_i, O_N, C_N, V_N, $R_{Ga}+Ga_i$, $R_{Ga}+N_i$, $R_{Ga}+O_N$, $R_{Ga}+V_{Ga}$, $R_{Ga}+V_N$	PP, DFTB	LDA, LDA+U	107, 111-113
$GaAs:Er^{3+}$	Er_{Ga}, $Er_{Ga}+O_{As}$, $Er_{Ga}+(O_{As})_2$, $Er_{Ga}+O_i$, $Er_{Ga}+O_{As}+O_i$	PP	LDA	114
$MAl_2O_4:Eu^{2+}$ (M: Ca, Sr, Ba)	Eu_M, V_{Sr}, V_{Al}, V_O	LAPW	GGA, GGA+U	II,IV
$SrAl_2O_4:Eu^{2+}$	Eu_{Sr}	n/a	n/a	115
$M_2MgSi_2O_7:Eu^{2+}$ (M: Ca, Sr, Ba)	Eu_M, V_{Sr}, V_{Mg}, V_{Si}, V_O, $V_{Sr}+V_O$, $Eu_{Sr}+V_{Sr}$, $Eu_{Sr}+V_O$	LAPW	LDA, LDA+U, GGA, GGA+U	III,V,VII
$Sr_2MgSi_2O_7:R^{2+/3+}$ (R: La-Lu)	R_M	LAPW	GGA, GGA+U	

The energies of the intrinsic (vacancies and interstitials) and extrinsic (foreign ions) bulk (Table 4) [116-130] and surface [81,131-150] defects (Table 5) in the electronic band structure of the host material have been studied using the DFT calculations. The electronic structure of the ideal and defect containing surfaces of the solid materials have been studied due to their importance for catalytic applications [*e.g.* 140,141,144]. The total and surface energies of the pure and defect containing materials have been calculated [116-120,123,125-150]. In addition, the formation and binding energies of the defects have been determined in order to study *e.g.* the probability of the defect formation in the bulk [116-130] and on the surface [81,139-150] of the host. The crystal structure of the defect containing materials has also been optimized to determine the structural modifications in the bulk and especially close to the surface due to the introduction of the defects [81,116-130,139-150].

Table 4. DFT studies of the electronic structure of intrinsic and extrinsic bulk defects in solid hosts.

Material	Defect	DFT calculation method	Exchange-correlation method	Ref.
AlN	V_N	LCAO	GGA	116
Si:B	B_{Si}, B_i, $B_{Si}+B_i$	PP	LDA, GGA	117
SiO_2:P	P_{Si}	Cluster	B3LYP	118
$Ca_3(PO_4)_2$	V_{Ca}	PP	LDA	119
$Ca_5(PO_4)_3OH$:Si	Si_P, Si_P+V_O, Si_P+V_{OH}	PP	LDA, GGA	120
TiO_2	V_O	PP	LDA	121
$SrTiO_3$	V_{Sr}, V_O, V_O+V_O	LCAO, PP, PAW	GGA, LDA, LDA+U, B3PW	122-124
ZrO_2, ZrO_2-Y_2O_3, ZrO_2-Sc_2O_3	V_O, O_i, V_O+Y_{Zr}, $Y_{Zr}+Y_{Zr}$	PP, PAW	GGA	125-127
CdO:F	F_O, V_O	PP	LDA	128
BaF_2	F_{Ba}, F_i	LCAO, PP	B3PW	129
HfO_2	V_O, O_i, V_{Hf}, Zr_{Hf}, V_O+Zr_{Hf}	PP	GGA	130

Table 5. DFT studies of the electronic structure of surfaces and surface defects.

	Material	Surface	Surface defect	DFT calculation method	Exchange-correlation method	Ref.
Ideal surface	MgO	(001)		LCAO	GGA	131
	$MgSiO_3$	(001), (110), (111), (101), (011)		PP	GGA	132
	SiO_2	(0001)		PP	LDA	133
	TiO_2	(110)		PP	LDA	134
	V_2O_5	(001), (100)		Cluster	GGA	135
	$SrTiO_3$	(001), (100)		LCAO, LMTO	LDA, GGA, B3PW, B3LYP	136,137
	$BaTiO_3$, $PbTiO_3$	(001)		LCAO	B3PW	136
	Ag-Pd heterostructure	(111)		PP	GGA	138
Defected surface	BN	(110)	V_B, V_N	LCAO	B3LYP	139
	MgO	(001)	Topological	PP	GGA	140
		(100)	V_O	Cluster	B3LYP	81,141
	MgO:Li	(100)	V_O	PP, PAW	GGA	142
		(100), (110), (111)	V_O, Li_i	PAW	GGA+U	143
	TiO_2	(110)	V_O	PAW	GGA+U	144
	NiO	(100)	V_{Ni}, V_O	PP, PAW	GGA, B3PW	145
	ZnO	(10-10), (11-20)	V_{Zn}, V_O	PP	GGA	146
	$SrTiO_3$	(001)	V_O	PP, PAW	GGA, B3PW	147
	CeO_2	(100), (110), (111)	V_O, V_O+V_O	PP, PAW	GGA, GGA+U	142, 148-150

The adsorption on the surface of a solid state substrate can be studied using DFT to explore the local surface environment involved in *e.g.* the actual catalytic processes [151]. The adsorption and dissociation energies of the atoms and molecules adsorbed on simple substrate materials as well as the total energies and electronic structures of these systems have been calculated (Table 6) [83,84,74,151-176]. The dependence of the adsorption energies and defect energies on the distance between the adsorbed species and the surface defects have been studied, as well [83,84,74,151,158-161,163,164,166-172,174]. The modification of the surface crystal structure due to the adsorption has been investigated using the structure optimization. In addition, the vibration frequencies of the adsorbed molecules [162,175] as well as the calculated electron paramagnetic resonance (EPR) spectra due to the paramagnetic surface defects [83,84,160] have been determined using the DFT calculations.

Table 6. DFT studies of surface adsorption and catalysis on inorganic substrate materials.

Substrate material	Adsorbed species	Surface defect	DFT calculation method	Exchange-correlation method	Ref.
Al	CH_3OH		PP	LDA	152
Si	F, Cl, OH, O_2		Cluster	GGA	153
	Ga, Te		PP	LDA	154-156
NaCl, KCl, $MgSO_4 \cdot H_2O$	Benzoic acid, salicylic acid		Cluster	B3LYP	157
MgO	H_2O, N_2O, OH, H_2, O_2, Li, Na, K	V_O	Cluster	B3LYP	83,84,74, 158-160
	Ca, Au	V_O	PAW	GGA	151,161
	CH_3OH		Cluster	B3LYP	162
	H_2S		PP	GGA	163
MgO:Ni	H_2S	Ni_{Mg}	PP	GGA	163
MgO:Li	CH_4	Li_{Mg}	PAW	GGA+U	164
SiO_2	H_2O		PP	GGA	165
SiO_2/Mo	Au	V_O	PAW	GGA	166
CaO	O_2	V_O	Cluster	B3LYP	159
TiO_2	H_2O, N_2O, N_2O_2, NO, CO, O_2, Au	V_O	PP	LDA, GGA	167-169
V_2O_5	H_2, CH_4, Li, Na, K, Rb	V_O	Cluster	LDA, GGA	170-172
ZnO	H_2S		PP	GGA	163
SrO	O_2	V_O	Cluster	B3LYP	159
Rh, Pd	CH_4, CO		PP	GGA	173
BaO	O_2	V_O	Cluster	B3LYP	159
CeO_2	NO_2	V_O	PAW	GGA+U	174
	CO		Cluster	B3LYP	175,176

3. EXPERIMENTAL

3.1. Materials Preparation

The polycrystalline $Sr_2MgSi_2O_7$ materials with or without Eu^{2+} and Dy^{3+} were prepared with a solid state reaction between stoichiometric amounts of $SrCO_3$, $Mg(NO_3)_2 \cdot 6H_2O$, fumed SiO_2, Eu_2O_3 and Dy_2O_3. The nominal concentration of both the Eu^{2+} and Dy^{3+} ions was 1 mole-% of the strontium amount. The dry starting materials were ground to a homogeneous mixture in a ball mill in air. The mixtures were annealed in a reducing (N_2 + 10 % H_2) gas sphere initially at 700 ^oC for 1 h and then at 1350 ^oC for 10 h. The structural and phase purity was confirmed by X-ray powder diffraction (XPD) using a Huber G670 image plate Guinier camera at 295 K (Cu $K_{\alpha 1}$ radiation, λ: 1.5406 Å).

3.2. Transmission Electron Microscopy

The nanostructure of the materials was studied at room temperature using a high-resolution JEOL JEM-3100FEF TEM system operated at 300 kV. For the TEM measurements the materials were dispersed into water and ultrasonically mixed for one hour at room temperature using a Branson 5510J-MTH ultrasonic cleaner. A drop of the suspension was then applied onto a copper grid sample holder and vacuum-dried for 12 h.

3.3. Thermoluminescence

The thermoluminescence glow curves of the $Sr_2MgSi_2O_7:Eu^{2+}(,Dy^{3+})$ materials were measured with an upgraded Risø TL/OSL-DA-12 TL system with a linear heating rate of 5 $°Cs^{-1}$ in the temperature range between 25 and 400 °C. The global TL emission from UV to 650 nm was monitored. Prior to the TL measurements, the materials were exposed to radiation from a combination of the Philips TL 20W/05 and TL 20W/03 UV lamps with the emission maxima at 360 and 420 nm, respectively. The exposure time was 30 s. The analysis of the TL glow curves was carried out by deconvoluting the TL curves with the program TLanal v. 1.0.3 [177,178] which uses the General Approximation method as a background. The fitted peaks were considered to be of either the 1st or 2nd order kinetics depending on the peak shape.

3.4. Luminescence Spectroscopy

The synchrotron radiation (SR) excitation and emission spectra of the $Sr_2MgSi_2O_7:Eu^{2+}(,Dy^{3+})$ materials were measured at 9 and 295 K in the energy range from 3.7 to 40 eV using the UV-VUV synchrotron radiation beamline SUPERLUMI of HASYLAB at DESY (Hamburg, Germany) [179]. The samples were mounted on the cold finger of a liquid He flow cryostat. The incident SR and the radiation emitted by the materials were dispersed with a 2-m normal incidence McPherson type primary monochromator and an ARC SpectraPro-308i monochromator equipped with a Hamamatsu R6358P photomultiplier, respectively. The luminescence was recorded with a SSL CCD detector, as well. The resolution of the experimental setup in excitation was between 0.02 and 0.32 nm depending on fixed slits. The UV–VUV excitation spectra were corrected for the incident flux variation of the excitation beam using the excitation spectrum of sodium salicylate as a standard. The measurements for a short (22 ns) and long (86 ns) time were carried out with a delay of 2 and 82 ns after the

excitation, respectively. The emission measurements are limited by the rather short time (192 ns) between the synchrotron radiation excitation pulses when compared to the conventional decay time of Eu^{2+} around 1 μs [180].

The UV excited emission spectra of the $Sr_2MgSi_2O_7$:Eu^{2+}(,Dy^{3+}) materials were measured at room temperature with a Perkin-Elmer LS-5 spectrometer (λ_{exc}: 360 nm). The excitation source was a pulsed 8 W xenon lamp.

3.5. Electronic Structure Calculations

The electronic structures of the non-doped and $R^{2+/3+}$ (R: La-Lu) doped $Sr_2MgSi_2O_7$ as well as non-doped and Eu^{2+} doped $SrAl_2O_4$ materials were calculated using the WIEN2k package [181]. WIEN2k is based on the full potential linearized augmented plane wave method (LAPW), an approach which is among the most precise and reliable ways to calculate the electronic structure of solids. The semi-local spin density generalized gradient approximation (GGA) method was employed. In order to describe better the strongly correlated 4f electrons of Eu^{2+}, the localized density approximation (LDA+U) and GGA+U methods [182,183] were used. These methods use the GGA (LDA) method, but for selected atomic states the DFT exchange-correlation potential is replaced by its Hartree-Fock-like form. The Coulomb interaction resulting in localized electronic states is correctly described with the exact exchange term in the Hartree-Fock approach, whereas exchange is only approximated in DFT. To correct for the double counting the "Fully Localized Limit" version of the GGA+U method was used.

The GGA+U and LDA+U methods require as the input the Coulomb repulsion strength (Hubbard parameter U) and the exchange parameter J (magnetic coupling constant), which can be related to the Slater integrals [184]. U increases with the increasing nuclear charge and oxidation state, whereas J is almost independent of the number of nd (nf) electrons. The U and J values 7.62 and 0.68 eV, respectively, have been found to reproduce the experimentally observed splitting between the majority and minority spin states of the Gd^{3+} ion [29]. Since both Gd^{3+} and Eu^{2+} have the rather similar $4f^7$ ground state configuration, the dependence of the Eu^{2+} doped system on the Hubbard parameter was calculated using selected U values between 4.35 and 7.62 eV, while the exchange parameter was fixed at 0.68 eV.

The GGA method was used for calculating the electronic structures of the $Sr_2MgSi_2O_7$:$R^{2+/3+}$ materials. The $4f^n$ electrons of the $R^{2+/3+}$ ions were treated as core electrons whereas 5d ones were included as valence electrons in the calculations. In this open core approach [185-187], the 4f electrons are coupled to the other electrons via Hartree and exchange interactions, but do not hybridize and are not part of the band structure. The f-character of the augmented plane waves at the R site was eliminated by setting the f-linearization energy at a high value (usually 25-80 eV). The 4f states were localized by a potential well and the occupation of the 4f(up) and 4f(down) spin states was fixed according to the first Hund rule. The open core approach was used to enable the reliable comparison between the calculated $4f^n$ ground state energies in the entire rare earth series. No charge compensation (not necessary for R^{2+}, of course) was included in the unit cell to account for the charge mismatch induced by the replacement of Sr^{2+} with an isolated R^{3+}. This omission

corresponds to an actual real situation where the charge compensation species is very far from the R^{3+} ion.

The isolated defects were calculated with no charge compensation included in the unit cell. One isolated defect was introduced into the normal unit cell of $Sr_2MgSi_2O_7$ (Z: 2 [188], 24 atoms) corresponding to the defect concentration of 25 (Eu_{Sr}^{x}, R_{Sr}^{x}, $R_{Sr}^{\bullet}$, $V_{Sr}^{''}$, and $V_{Si}^{''''}$; one of the four Sr^{2+}/Si^{IV} species in the unit cell is replaced with a defect), 50 ($V_{Mg}^{''}$), and 7 % ($V_{O}^{\bullet\bullet}$). The high local defect concentrations were used to probe the local changes in the electronic structure induced by the isolated defects. One isolated oxygen vacancy was also located in a 2x2x2 supercell of $Sr_2MgSi_2O_7$ (a: 15.9914, c: 10.3042 Å, 192 atoms) corresponding to a 1 % $V_{O}^{\bullet\bullet}$ concentration. One isolated defect was introduced in the normal unit cell of $SrAl_2O_4$ (Z: 4 [189], 28 atoms), as well, corresponding to the defect concentration of 25 (Eu_{Sr}^{x} and $V_{Sr}^{''}$; one of the four Sr^{2+} ions in the unit cell is replaced), 13 ($V_{Al}^{'''}$), and 6 % ($V_{O}^{\bullet\bullet}$).

Selected defect aggregates with the defects at the closest possible distance relative to each other ($V_{Sr}^{''} + V_{O}^{\bullet\bullet}$ and $Eu_{Sr}^{x} + V_{Sr}^{''}$) or at different distances ($Eu_{Sr}^{x} + V_{O}^{\bullet\bullet}$, 2.6-7.2 Å) were calculated in the $Sr_2MgSi_2O_7$ host, as well. The $V_{Sr}^{''} + V_{O}^{\bullet\bullet}$ and $Eu_{Sr}^{x} + V_{O}^{\bullet\bullet}$ pairs were located in a 1x1x3 supercell (a: 7.9957, c: 15.4563 Å, 72 atoms) corresponding to the defect concentration of 8 (Eu_{Sr}^{x} and $V_{Sr}^{''}$) and 2 % ($V_{O}^{\bullet\bullet}$). The $Eu_{Sr}^{x} + V_{Sr}^{''}$ pair was introduced in a 1x1x2 supercell (a: 7.9957, c: 10.3042 Å, 48 atoms) corresponding to a 13 % Eu_{Sr}^{x} and $V_{Sr}^{''}$ concentration. The Eu^{2+} $4f^7$ electrons were treated as core electrons in the $Eu_{Sr}^{x} + V_{Sr}^{''}$ pair since the GGA+U method failed to describe them correctly. This may be due to the insufficient handling of the charge misbalance induced by the introduction of $V_{Sr}^{''}$ in the lattice.

The single particle Kohn-Sham equations can be solved on a grid of sampling points (k-points) in the symmetry irreducible wedge of the Brillouin zone [24]. The number of the *k*-points in the irreducible part of the Brillouin zone of $Sr_2MgSi_2O_7$ ($SrAl_2O_4$) was 12 (16) and 6 (8) with and without the spin-orbit coupling included, respectively. The number of basis functions used was *ca.* 1500 and 1800 for both the non-doped and defect containing normal cell of the $Sr_2MgSi_2O_7$ and $SrAl_2O_4$ materials, respectively. The number of basis functions was significantly higher in the $Sr_2MgSi_2O_7$ supercell calculations, *ca.* 3100 (1x1x2 supercell), 4600 (1x1x3) and 9200 (2x2x2).

The reliable calculation of the electronic structure requires the optimization of the crystal structure including the defect or defect aggregate. This was achieved by relaxing the atomic positions in the unit cell, while the lattice parameters were not changed. The equilibrium position of each atom was calculated using the GGA method. The optimized structure was then used to recalculate the electronic structure by employing the GGA or GGA+U method without the spin-orbit coupling.

4. RESULTS AND DISCUSSION

4.1. Crystal Structure

4.1.1. $Sr_2MgSi_2O_7$

X-ray powder diffraction was used to confirm the structural and phase purity of the materials (Fig. 3) [VI]. All the $Sr_2MgSi_2O_7$ materials studied possess the tetragonal structure (space group: $P\bar{4}2_1m$, no. 113, Z: 2, a: 7.9957, c: 5.1521 Å [188]). The structure consists of alternating Sr and $Mg(Si_2O_7)$ layers perpendicular to the unit cell c axis (Fig. 4). The distance between the Sr planes (002) is 5.15 Å along the unit cell c axis, while the shortest distance between two Sr atoms in the ab plane is 3.74 Å. The structure possesses only one Sr, Mg and Si site but three O sites. The oxide ion in the O1 site connects two SiO_4 tetrahedra into a disilicate (Si_2O_7) unit. The Sr^{2+} ion in the single Sr site (symmetry: C_s) has eight neighboring O^{2-} ions with an average Sr-O distance of 2.662 Å. The Mg^{2+} and Si^{IV} species are located within the MgO_4 and SiO_4 tetrahedra (site symmetries: S_4 and C_s, respectively) with average Mg-O and Si-O distances of 1.942 and 1.617 Å, respectively. In addition to the desired $Sr_2MgSi_2O_7$ phase, a small amount of $Sr_3MgSi_2O_8$ was observed as an impurity phase in the XPD patterns of all materials at room temperature. The decrease in the intensities of the reflections of the $Sr_3MgSi_2O_8$ impurity phase compared to $Sr_2MgSi_2O_7$ indicated that the introduction of the Eu^{2+} and Dy^{3+} ions favors the formation of the desired $Sr_2MgSi_2O_7$ phase.
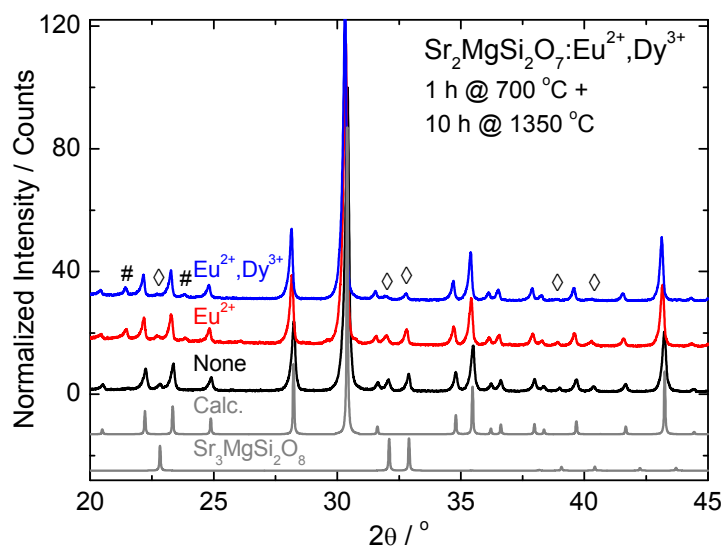
Figure 3. Experimental X-ray powder diffraction patterns of the non-doped and Eu^{2+} doped as well as Eu^{2+},Dy^{3+} co-doped (1 mole-% both Eu^{2+} and Dy^{3+}) $Sr_2MgSi_2O_7$ at 295 K. Impurity and Vaseline (used to attach the sample) reflections: $\Diamond$ $Sr_3MgSi_2O_8$ (2θ: 22.6^o (I/I_{100}: 0.4); 31.8 (0.8); 32.7 (1); 38.8 (0.4); 40.3 (0.55)), # Vaseline. The reference pattern was calculated with PowderCell [190] using the crystallographic data [188].

24
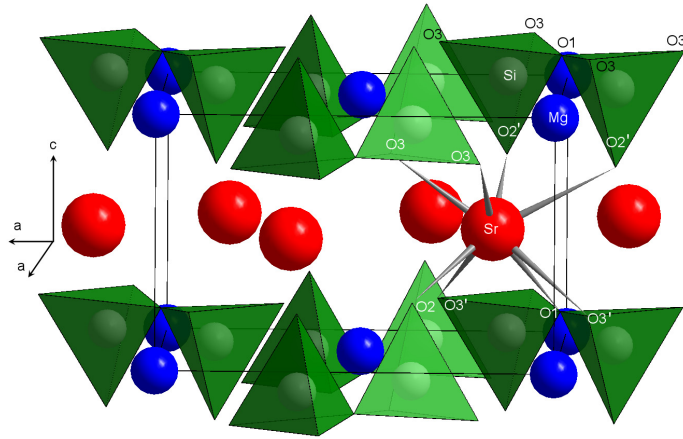
Figure 4. The tetragonal structure (space group $P\bar{4}2_1m$) of $Sr_2MgSi_2O_7$ consisting of alternating Sr and $Mg(Si_2O_7)$ layers.

4.1.2. SrAl₂O₄

The $SrAl_2O_4$ materials studied possess the monoclinic structure (space group: $P2_1$, no. 4, Z: 4, a: 8.447, b: 8.816, c: 5.163 Å and β: 93.4° [189]). The structure consists of Sr^{2+} ions situated within channels formed by six interconnected AlO_4 tetrahedra (Fig. 5). The structure possesses two Sr, four Al and eight O sites. The Eu^{2+} ion is expected to substitute for Sr^{2+} in both seven coordinated sites (Sr1 and Sr2, C_1 site symmetry for both) since the Sr-O distances (average: 2.692 and 2.667 Å for Sr1 and Sr2, respectively) are very similar [IV]. In addition, the statistical ionic radii of Eu^{2+} (CN: 7, 1.20 Å) and Sr^{2+} (1.21 Å) are close to a perfect match [191]. In contrast, Eu^{2+} does not fit at all into the small four coordinated Al^{3+} site (0.39 Å).
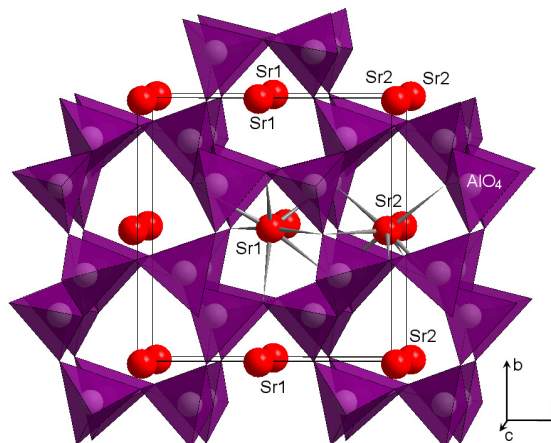
Figure 5. The monoclinic structure (space group $P2_1$) of $SrAl_2O_4$ consisting of Sr^{2+} ions situated within channels of AlO_4 tetrahedra.

4.2. Microscopic Structure

High-resolution transmission electron microscopy was used to study the modification of the local crystal structure induced by the lattice defects in the polycrystalline materials. Undisturbed Sr crystal planes were typically observed in the non-doped $Sr_2MgSi_2O_7$ material (Fig. 6) [I]. The Sr planes with

a distance of 5.15 (Fig. 6a) and 3.74 Å (Fig. 6c) along the unit cell c axis and in the ab plane, respectively (*cf.* section 4.1.1.), were observed. Dislocations and other infrequent discontinuities were found even in the non-doped material, however. Small lattice domains with different crystal plane orientations were observed, as well. This indicates that lattice defects exist in the $Sr_2MgSi_2O_7$ material even without (co-)doping. A significant number of discontinuities in the crystal planes as well as increasingly smaller domains with different lattice orientations were clearly observed for the Eu^{2+} doped and Eu^{2+},Dy^{3+} co-doped $Sr_2MgSi_2O_7$ materials. The domains are probably created by point defects or defect aggregates. The edges of the domains may also consist of dislocations which have their origin at the point defects.
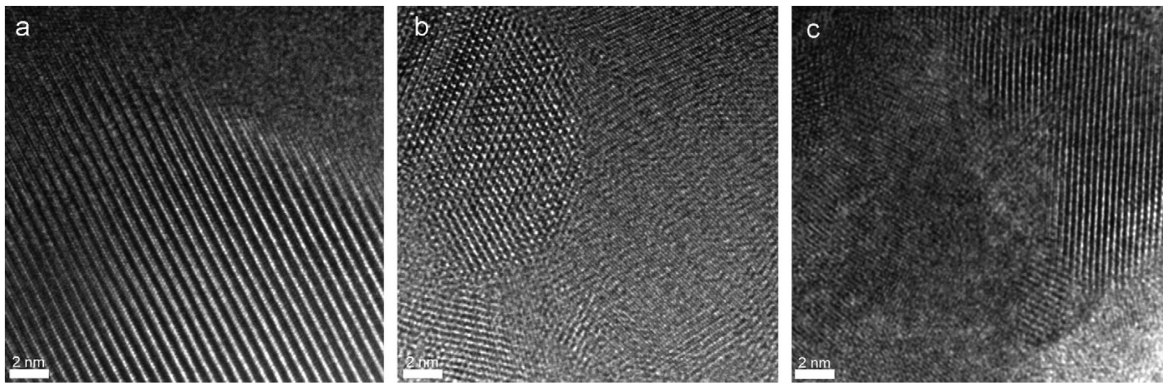
Figure 6. Transmission electron microscopy (TEM) images of a) $Sr_2MgSi_2O_7$, b) $Sr_2MgSi_2O_7$:Eu^{2+} and c) $Sr_2MgSi_2O_7$:Eu^{2+},Dy^{3+}.

Eu^{2+} replaces Sr^{2+} in the single Sr site of the $Sr_2MgSi_2O_7$ host without major structural distortions (ionic radii: 1.25 and 1.26 Å [191], respectively, see also section 4.1.2.). The eight coordinated Dy^{3+} ion (1.03 Å) fits rather well into the Sr^{2+} site, whereas Eu^{2+} and Dy^{3+} do not fit at all into the small four coordinated Mg^{2+} and Si^{IV} sites (0.57 and 0.26 Å, respectively). The replacement of Sr^{2+} with Dy^{3+} ($Dy_{Sr}^{\bullet}$) is expected to modify the host structure due to their size mismatch. In addition, strontium vacancies ($V_{Sr}^{''}$) and/or interstitial oxide ions ($O_i^{''}$) may be created to provide the charge compensation required by the introduction of an extra positive net charge with $Dy_{Sr}^{\bullet}$ (Eqs. 5 and 6).

$$2Sr^{2+} \rightarrow 2Dy_{Sr}^{\bullet} + V_{Sr}^{''} \qquad (5)$$
$$2Sr^{2+} \rightarrow 2Dy_{Sr}^{\bullet} + O_i^{''} \qquad (6)$$

In addition to the isolated lattice defects, aggregation of defects has to be considered since the actual defect concentration is expected to be quite significant because of the high energy storing capacity of the materials. Especially the Eu^{2+},Dy^{3+} co-doped material is expected to contain a large number of defect aggregates. The negatively charged defects $V_{Sr}^{''}$ and $O_i^{''}$ are able to aggregate with the positively charged defects $V_O^{\bullet\bullet}$ and/or $Dy_{Sr}^{\bullet}$ thus increasing the local defect concentration. The increased disorder observed in the TEM images of the (co-)doped material (Fig. 6) is thus mainly due to the charge compensation effects [I].

4.3. Structure Optimization

4.3.1. Eu^{2+} Doped $Sr_2MgSi_2O_7$

The DFT calculations provide an important tool to study the modification of the crystal structure due to the introduction of the isolated defects and defect aggregates since both the nature of the defects and the distance between them can be exactly determined. These modifications induced by the isolated defects were first studied using the Eu^{2+} doped $Sr_2MgSi_2O_7$, *i.e.* with the Eu_{Sr}^{x} defect with no net charge [V,VII]. Due to the structure optimization, the distances between the Eu^{2+}/Sr^{2+} ions and the nearest oxide ions were decreased. The modification of the crystal structure was slightly more pronounced around the Eu^{2+} luminescent centre than near the Sr^{2+} ions. The average decrease in the Eu-O and Sr-O distances was 0.018 and 0.013 Å, respectively. The average changes relative to the non-optimized distances are thus 0.7 and 0.5 %, respectively. In addition, the Mg-O distances decreased in average 0.002 Å (0.1 %). The decrease in the Eu-O, Sr-O and Mg-O distances takes place at the expense of lengthening of the Si-O distances, in average increased by 0.028 Å (1.7 %).

4.3.2. Isolated Vacancies and Defect Aggregates in $Sr_2MgSi_2O_7$

The probability of the formation of the defect species increases with the decreasing total energy. The structural modifications in $Sr_2MgSi_2O_7$ induced by the Sr vacancy are more profound than the effect of $V_{Mg}^{''}$, $V_{Si}^{''''}$ and $V_O^{\bullet\bullet}$ [VII]. This is reflected by the differences in the total energies of the defect free and vacancy containing $Sr_2MgSi_2O_7$ (Fig. 7). The difference in the total energies (85 keV) show that the formation of $V_O^{\bullet\bullet}$ in the O1, O2 and O3 oxygen sites requires much less energy than the creation of $V_{Sr}^{''}$. Therefore, $V_O^{\bullet\bullet}$ may be formed relatively easily due to the reducing atmosphere used in the materials preparation.
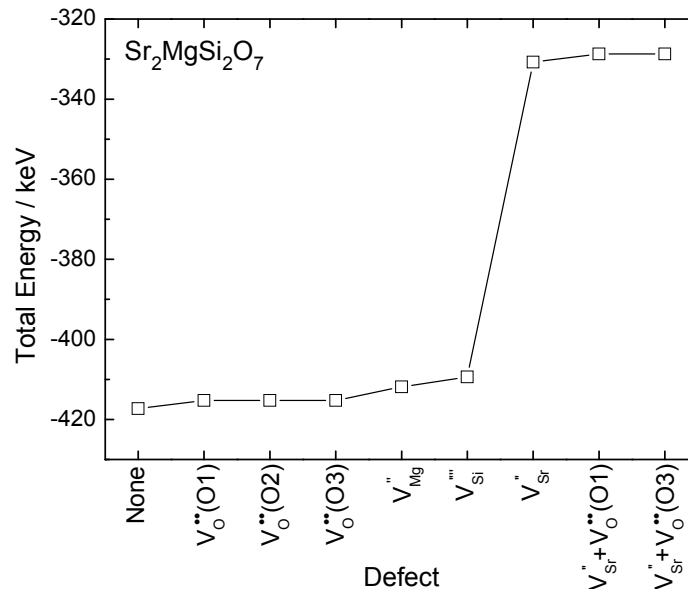
Figure 7. Total energy of the optimized $Sr_2MgSi_2O_7$ structure with isolated defects and defect aggregates in the normal unit cell calculated with the GGA method.

The probability of the formation of $V_{Mg}^{''}$ and $V_{Si}^{''''}$ cannot be estimated reliably using only the total energy values (Fig. 7) since their structural effects may be more significant than indicated by the

present DFT calculations [VII]. In addition, the charge compensation required by V_{Si}'''' with a quadruple negative net charge should introduce additional defects and thus increase the total energy. The total energy of the Eu^{2+} containing $Sr_2MgSi_2O_7$ material cannot be compared with the non-doped and vacancy containing material due to its strong dependency on the atomic number. Therefore, the total energy is drastically changed (by *ca.* 210 keV) with the replacement of Sr^{2+} with Eu^{2+}.

Based on the changes in the Sr-O and Eu-O distances, the structural modifications due to the isolated vacancies are much more significant than the inclusion of the Eu^{2+} ion alone (Table 7) [VII]. The modifications induced by the removal of an oxygen in the O1 site are also more significant than in the O2 and O3 sites due to its role as the central atom of the Si_2O_7 unit (*cf.* section 4.1.1.). The changes in the interionic distances in the environment of the defect pairs $Eu_{Sr}^x + V_{Sr}''$, $Eu_{Sr}^x + V_O^{\bullet\bullet}$, and $V_{Sr}'' + V_O^{\bullet\bullet}$ were studied using the structure optimization. In this process, the O^{2-} ions located between Eu^{2+} and V_{Sr}'' in the $Eu_{Sr}^x + V_{Sr}''$ pair moved most strongly towards Eu^{2+}. The modification of the environment due to V_{Sr}'' in the $Eu_{Sr}^x + V_{Sr}''$ defect pair agrees very well with the changes in the crystal structure induced by the isolated V_{Sr}''. The introduction of the $Eu_{Sr}^x + V_O^{\bullet\bullet}$ pair decreased the remaining Eu-O distances. Significant decrease in the Eu-O distances was observed when Eu^{2+} and $V_O^{\bullet\bullet}$ are located as nearest neighbors. On the other hand, the modifications are clearly less significant when $V_O^{\bullet\bullet}$ is located at longer distances from Eu^{2+}. These results confirm that the aggregation of defects can significantly modify the local crystal structure of the host material.

Table 7. Average decrease in the Sr-O and Eu-O distances in the isolated defect and defect aggregate containing $Sr_2MgSi_2O_7$.

Defect	Distance* / Å	Sr-O or Eu-O distance Decrease[#]	
		/ Å	/ %
Eu_{Sr}^x		0.013 (Sr-O)	0.5
V_{Sr}''		0.110	4.0
V_{Mg}''		0.073	2.7
V_{Si}''''		0.006	0.2
$V_O^{\bullet\bullet}$ (O1)		0.076	2.8
$V_O^{\bullet\bullet}$ (O2)		0.049	1.8
$V_O^{\bullet\bullet}$ (O3)		0.041	1.5
$V_{Sr}'' + V_O^{\bullet\bullet}$ (O1)	2.58	0.006	0.2
$V_{Sr}'' + V_O^{\bullet\bullet}$ (O3)	2.77	0.004	0.1
$Eu_{Sr}^x + V_O^{\bullet\bullet}$ (O1)	2.58	0.080 (Eu-O)	2.9
	5.11	0.022	0.8
	7.18	0.019	0.7
$Eu_{Sr}^x + V_O^{\bullet\bullet}$ (O3)	2.77	0.042	1.6
	5.68	0.019	0.7
	7.12	0.020	0.7
$Eu_{Sr}^x + V_{Sr}''$	4.22	0.090	3.4

* Distance between defects in the defect aggregate.

[#] Decrease from the non-optimized average distance (2.662 Å) due to structure optimization.

The $V_{Sr}'' + V_O^{\bullet\bullet}$ pair induced only very slight structural modifications when compared to the changes caused by the isolated vacancies (Table 7) [VII]. This may result from the inherent charge compensation of the $V_{Sr}'' + V_O^{\bullet\bullet}$ pair which might stabilize the environment of the pair. The total energies indicate that the energy cost of creating the $V_{Sr}'' + V_O^{\bullet\bullet}$ pair is similar to the cost of creating the corresponding isolated vacancies (Fig. 7).

4.3.3. $R^{2+/3+}$ Doped $Sr_2MgSi_2O_7$

The crystal structure of the La^{3+} and Lu^{3+} (in the sole Sr site) containing $Sr_2MgSi_2O_7$ was optimized. Assuming that in the rare earth series the dependence of structure parameters on the R atomic number is linear, the optimized structure was constructed for the Ce^{3+}-Yb^{3+} containing material using linear interpolation. The shortest average R-O distance, 2.439 Å for the Lu^{3+} doping, corresponds to an 8 % decrease from the original Sr-O distance of 2.662 Å. The Lu^{3+} $4f^{14}$ ground state energy increases only by *ca.* 0.2 eV whilst smaller changes were found for the other R^{3+} due to the optimization (*cf.* section 4.4.6.). Therefore, the non-optimized crystal structure was used in the DFT calculations of the R^{3+} and R^{2+} doped $Sr_2MgSi_2O_7$. The total energy of the $R^{2+/3+}$ containing $Sr_2MgSi_2O_7$ materials are not comparable due to the strong dependency of this energy on the number of electrons.

4.3.4. Eu^{2+} Doped $SrAl_2O_4$

The Eu-O distances were slightly shorter in the optimized structure than the original Sr-O distances when the crystal structure of the Eu^{2+} doped $SrAl_2O_4$ material was optimized with the DFT calculations [II,IV]. The average change in the Eu-O (Sr-O) distance is 0.038 or 0.027 Å (0.029 or 0.021 Å), when Eu^{2+} is located in the Sr1 or Sr2 site, respectively (IV, Table 1). This decrease takes place at the expense of the lengthening Al-O distances, in average increased by 0.017 Å. The average changes relative to the non-optimized distances are thus similar for Sr(Eu)-O and Al-O, 0.8-1.4 and 1.0 %, respectively. Based on the smaller decrease in Eu-O and Sr-O distances (0.7 and 0.5 % for $Sr_2MgSi_2O_7$, respectively, *cf.* section 4.3.1.), the $Sr_2MgSi_2O_7$ structure is more rigid than $SrAl_2O_4$.

In the Sr1 site, two types of oxide ion movement – changes in both the O-Eu-O angles and the Eu-O distances – exist due to optimization (Fig. 8) [IV]. The differences between the non-optimized and optimized crystal structure are small, although even smaller changes might have been expected due to the similar statistical ionic radii of Eu^{2+} and Sr^{2+}. Since the tabulated ionic radii are statistical ones, the actual inter-atomic distances may differ in the individual materials, however.
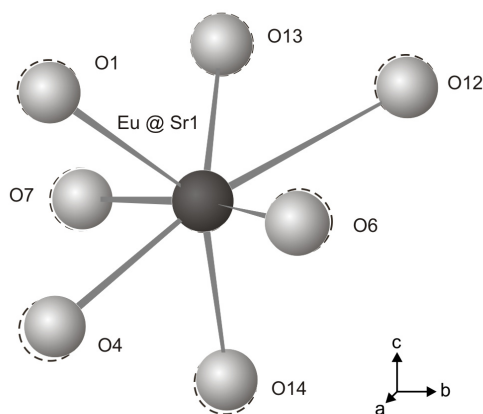
Figure 8. Environment of Eu^{2+} in the Sr1 site of the structure optimized $SrAl_2O_4$:Eu^{2+}. Non-optimized ion positions are marked with dashed spheres.

4.3.5. Isolated Vacancies in $SrAl_2O_4$

The introduction of a strontium vacancy in $SrAl_2O_4$ results in the movement of the nearest-neighbor O^{2-} ions towards the next-nearest Sr^{2+} ions due to the structure optimization. The resulting average decrease in the Sr-O distances is 0.129 and 0.151 Å for $V_{Sr}^{"}$ in the Sr1 and Sr2 site, respectively. The average changes relative to the non-optimized distances are 4.8 and 5.2 %, respectively. The effect of $V_{Sr}^{"}$ to the crystal structure of $SrAl_2O_4$ is much more profound than that of $V_O^{\bullet\bullet}$. The average decrease in the Sr-O distances for the nearest-neighbor Sr^{2+} ion due to $V_O^{\bullet\bullet}$ is 0.034 Å (1.2 %). These values are in good agreement with the local modifications induced by the introduction of $V_{Sr}^{"}$ and $V_O^{\bullet\bullet}$ in $Sr_2MgSi_2O_7$. The Al-O distances were not changed due to the introduction of $V_{Sr}^{"}$ or $V_O^{\bullet\bullet}$.

The total energies of the defect free and $V_O^{\bullet\bullet}$, $V_{Al}^{'''}$ or $V_{Sr}^{"}$ containing $SrAl_2O_4$ material are *ca.* -432, -430, -425 or -345 keV, respectively. Therefore, $V_O^{\bullet\bullet}$ may be formed relatively easily also in $SrAl_2O_4$ due to the reducing atmosphere used in the materials preparation. In addition, the high energy cost of the formation of $V_{Sr}^{"}$ may indicate that a high temperature is required for the evaporation of SrO from this material.

4.4. Electronic Structure

4.4.1. Host Band Structure of $Sr_2MgSi_2O_7$

The electronic band structure along a high symmetry path in the first Brillouin zone as well as the density of states (DOS) of the non-doped $Sr_2MgSi_2O_7$ host was calculated as the starting point of the DFT studies (Fig. 9) [VII]. The minimum of the conduction band (CB) is located at the origin of the Brillouin zone (Γ point) at 4.8 eV above the maximum of the valence band (VB). The maximum of VB does not occur at the Γ point but is located instead at the Brillouin zone boundary (Z point) indicating an indirect band gap. However, the energy difference of the maximum of VB between the Γ and Z points is only *ca.* 0.3 eV.
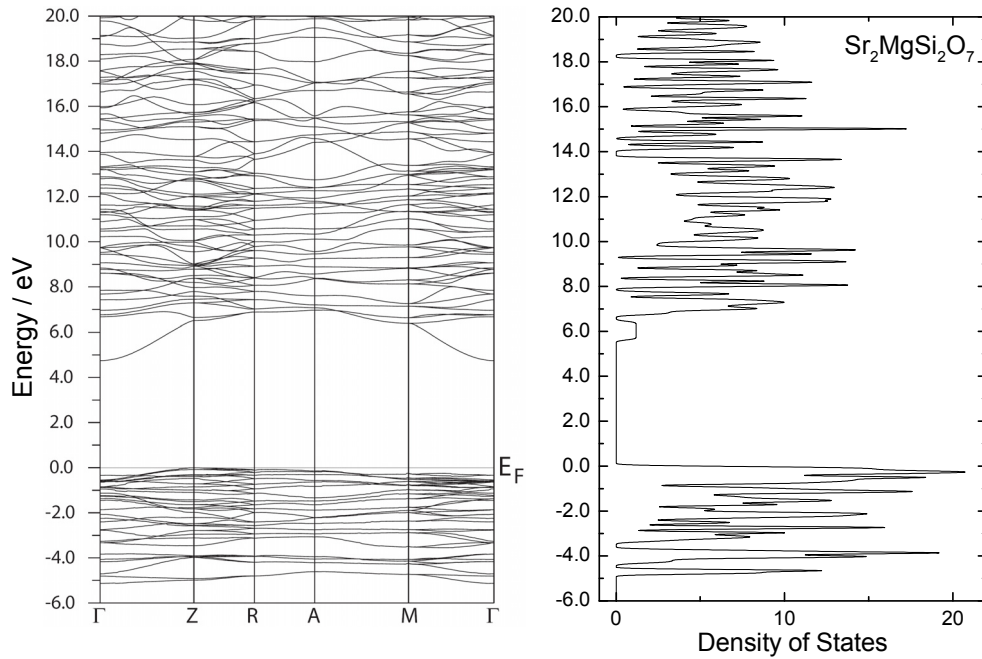
Figure 9. Calculated (GGA method) band structure along a high symmetry path in the first Brillouin zone (left) and total density of states of $Sr_2MgSi_2O_7$ (right) (E_F: Fermi energy).

The DFT calculations did not provide an absolute measure for the band gap energy (E_g) due to the presence of scattered non-zero density of states (DOS) from 4.8 eV above the top of VB (Fig. 9) [III,VII]. This might suggest the presence of an intrinsic electron trap even in the defect free $Sr_2MgSi_2O_7$, though no discrete state is found. A significant increase in the DOS appears at 6.7 eV (Figs. 9 and 10). This increase may be used as a more reliable measure for the band gap energy than the scattered DOS at lower energy. Therefore, the derivative curves of both the excitation spectrum and the calculated total DOS were used to obtain accurate and comparable E_g values (Fig. 11). The agreement between the experimental (7.1 eV, see also section 4.6.) and calculated (6.7 eV) values is very good. The difference of 0.4 eV is not important when the experimental uncertainties are taken into account. Generally, the discrepancy amounts to 1 eV or more [50,55].
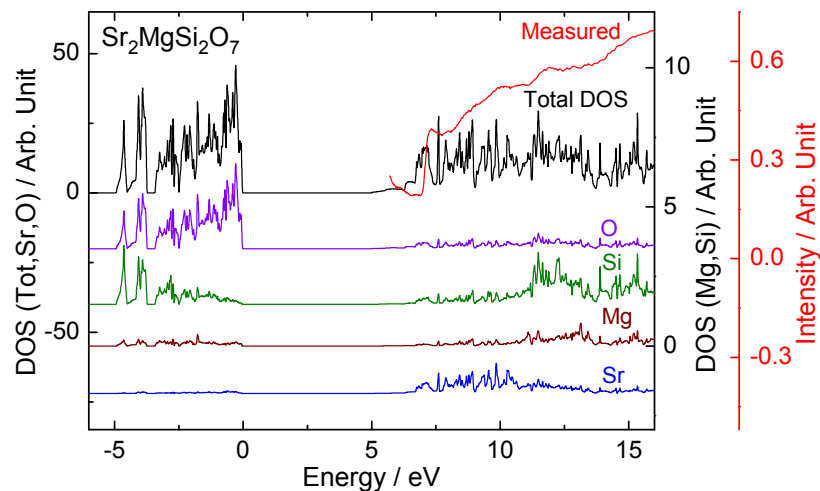
Figure 10. Calculated (GGA method) density of states of the non-doped $Sr_2MgSi_2O_7$ with the UV-VUV synchrotron radiation excitation spectrum of $Sr_2MgSi_2O_7:Eu^{2+}$ at 10 K (λ_{em}: 470 nm).
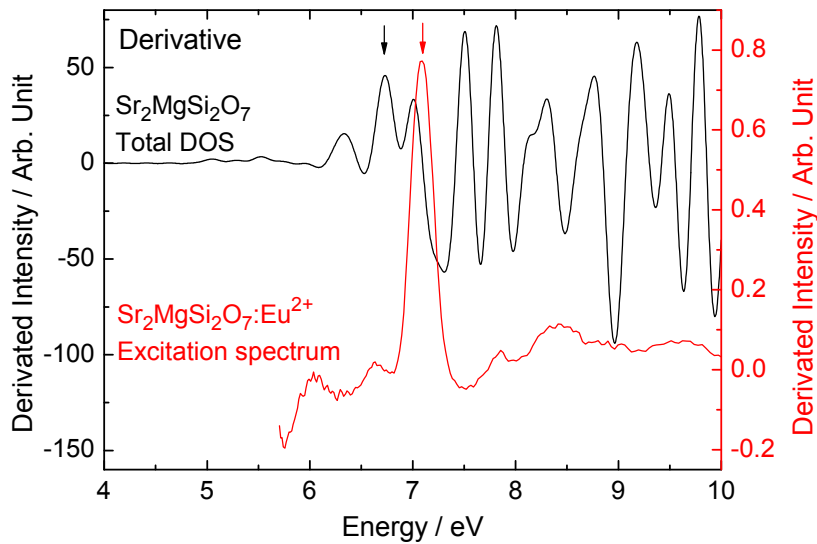
Figure 11. Derivative curves of the calculated (GGA method) DOS of $Sr_2MgSi_2O_7$ and the UV-VUV excitation spectrum of $Sr_2MgSi_2O_7:Eu^{2+}$ at 10 K (λ_{em}: 470 nm, the arrows indicate E_g).

The valence band of $Sr_2MgSi_2O_7$ has mainly the O(2p) character (Figs. 10 and 12) [III,VII]. The DOS originating from the oxygen in the O3 site are distributed evenly across the main VB between 0 and 5 eV below the Fermi level. The bottom and top of the VB have a pronounced oxygen character originating from the oxygen in the O1 and O2 sites, respectively. The lower part of the conduction band from 7 to 13 eV consists mostly of the Sr(4d) states. The maximum density of the Mg and Si states as well as the Sr(5p) states is located deep (above 11 eV) in the conduction band (Fig. 10). These results indicate that the introduction of $V_O^{\bullet\bullet}$ does not have a significant effect on the conduction band. In addition, V_{Mg}'' and V_{Si}'''' would not have an effect on the lower part of CB.
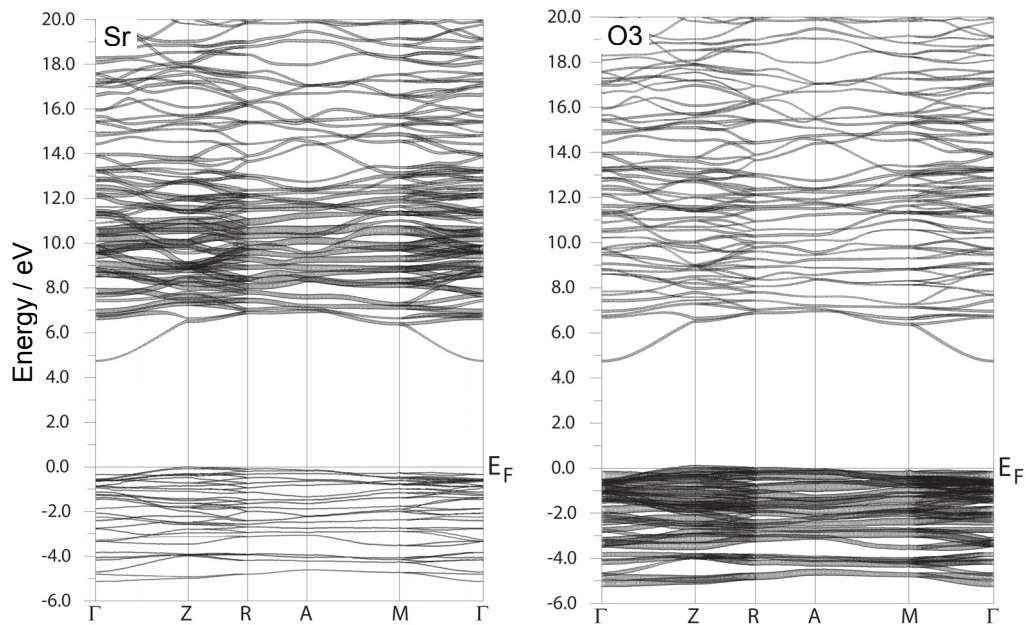
Figure 12. Calculated (GGA method) band structure of $Sr_2MgSi_2O_7$ including the states with strontium (left) and oxygen (O3 site, right) character indicated by the heavier plotting (E_F: Fermi energy).

4.4.2. Host Band Structure of SrAl₂O₄

For the non-doped $SrAl_2O_4$ material, the E_g value of 6.4 eV was obtained from the derivative curve [II]. The agreement between the experimental (6.6 eV) and calculated values is very good and the difference of 0.2 eV is insignificant. This shows a considerable improvement to an earlier theoretical GGA approach [55], where a largely underestimated E_g value of 4.5 eV was reported for $SrAl_2O_4$. A local maximum in the DOS is found at *ca.* 1.5 eV below CB (Fig. 13). This may indicate the presence of an intrinsic shallow electron trap which exists even without the introduction of any defects in this material.
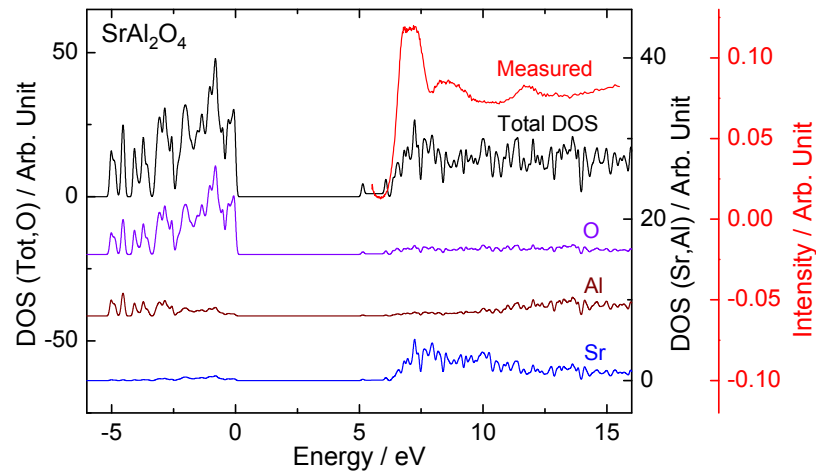
Figure 13. Calculated (GGA method) density of states and the UV-VUV synchrotron radiation excitation spectrum (at 10 K, λ_{em}: 320 nm) of the non-doped $SrAl_2O_4$.

According to the DFT calculations, the valence band of $SrAl_2O_4$ has mainly the O(2p) character, whereas the bottom of the conduction band consists mostly of the Sr states (Fig. 13) [II]. Most of the Al DOS is located deep in the conduction band. The structure of the valence and conduction band as well as the E_g value did not change from the non-doped $SrAl_2O_4$ whether the optimized or non-optimized crystal structures of the Eu^{2+} doped material were used (Fig. 14).
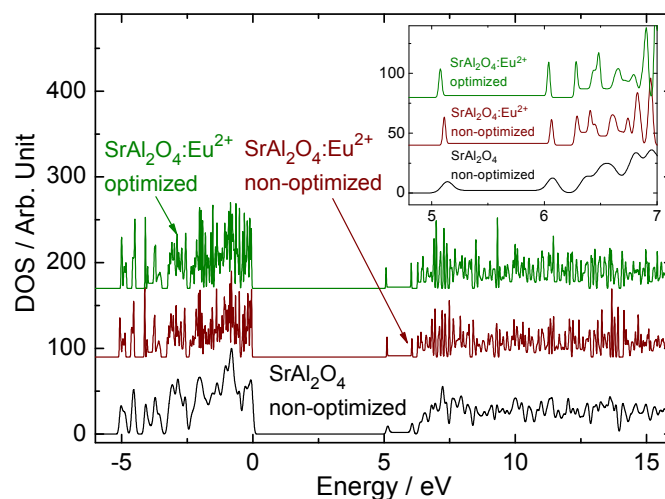
Figure 14. Calculated density of states of the non-optimized $SrAl_2O_4$ (GGA) and non-optimized as well as optimized $SrAl_2O_4$:Eu^{2+} (GGA+U method, *U*: 7.62 eV) without the Eu^{2+} $4f^7$ $^8S_{7/2}$ ground state.

4.4.3. $4f^7$ Ground State of Eu^{2+}

The Eu^{2+} doping did not change the E_g value in $Sr_2MgSi_2O_7$ [III] or $SrAl_2O_4$ [II,IV]. E_g was found to be independent of the Coulomb repulsion strength (U was varied in the range of 4.35-7.62 eV) and of structure optimization. In addition, E_g did not change with the introduction of Eu^{2+} in the Sr1 or Sr2 site in $SrAl_2O_4$. A local maximum of DOS is found at *ca.* 1.5 eV below CB for both $Sr_2MgSi_2O_7$:Eu^{2+} and $SrAl_2O_4$:Eu^{2+} (Fig. 15) [II-IV]. The electron trap corresponding to this maximum may help to explain the persistent luminescence observed from the disilicate and aluminate materials even without the R^{3+} co-doping.
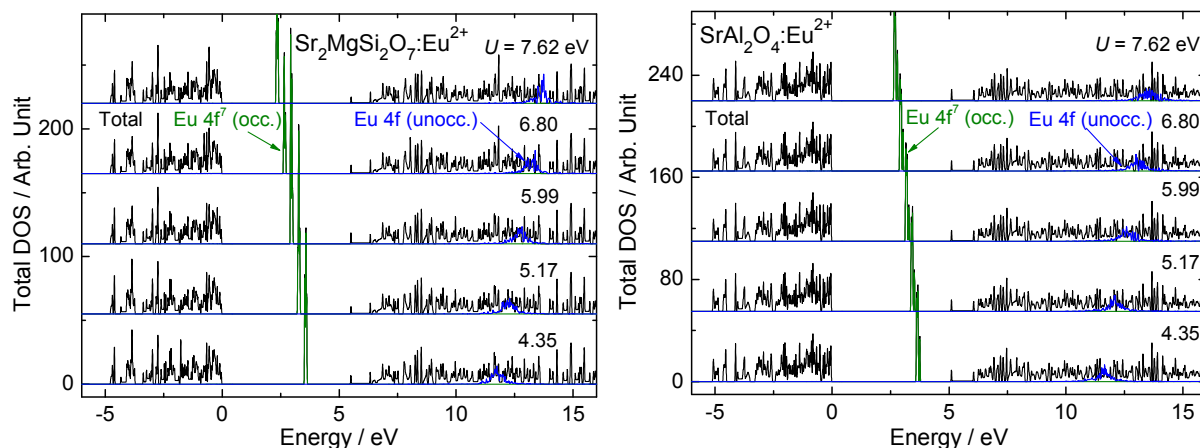
Figure 15. Dependence of the calculated (GGA+U method, U: 4.35-7.62 eV) density of states of the non-optimized $Sr_2MgSi_2O_7$:Eu^{2+} and $SrAl_2O_4$:Eu^{2+} (Eu^{2+} in the Sr1 site) on the Coulomb repulsion strength.

The position of the $4f^7$ $^8S_{7/2}$ ground state of Eu^{2+} plays a major role in the persistent luminescence processes since both the $4f^7 \rightarrow 4f^65d^1$ photoexcitation and the $4f^65d^1 \rightarrow 4f^7$ photoemission of Eu^{2+} involve this state. The position of the $4f^7$ ground state can be experimentally determined when the Eu^{3+} charge transfer (CT) energy is known. However, there always remains an uncertainty of *ca.* 0.5 eV due to the broad band nature of the CT absorption. Similar CT energy values have been observed for europium in the disilicate or aluminate materials (5.0 and 4.9 eV for $Sr_2MgSi_2O_7$:Eu^{3+} [192] and $CaAl_2O_4$:Eu^{3+} [14], respectively). This transition energy is approximately the same as the energy difference between the top of VB and the $4f^7$ ground state of the Eu^{2+} ion [15] locating it in the energy gap.

The occupied (majority spin) Eu^{2+} $4f^7$ ground state lies in the energy gap of both the $Sr_2MgSi_2O_7$ [III] and $SrAl_2O_4$ [II,IV] host irrespective of the value of the Hubbard parameter used in the DFT calculations (Fig. 15). The basic requirement for the successful calculation of the electronic structure of the Eu^{2+} doped disilicate and aluminate materials was thus fulfilled.

The dependence of the $4f^7$ ground state energy on U is linear, with this state located closer to the valence band for the higher U values (Fig. 16) [II,III]. The calculated energy difference between the top of VB and the $4f^7$ ground state position of Eu^{2+} is 2.3-3.6 and 2.7-3.7 eV for $Sr_2MgSi_2O_7$:Eu^{2+} and $SrAl_2O_4$:Eu^{2+}, respectively. The $4f^7$ ground state positions are underestimated by *ca.* 2 eV when compared to the experimental CT values. However, the experimental CT energy may significantly

overestimate the $4f^7$ position due to its relaxation after the CT absorption. Nevertheless, the strong U dependence provides a challenge in determining the absolute position of the $4f^7$ ground state since a reliable calculation of the U parameter (and J, too) value was not found possible with the present DFT studies.
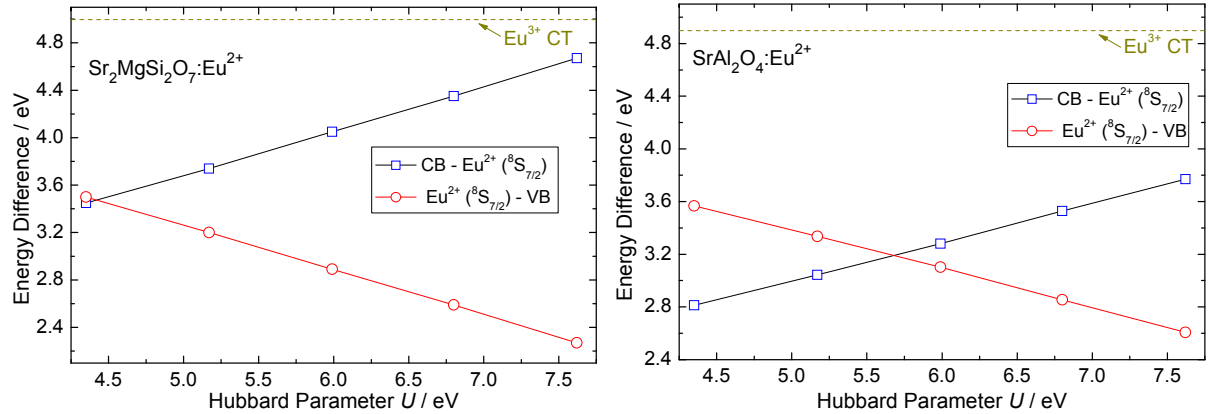
Figure 16. Calculated (GGA+U method, U: 4.35-7.62 eV) energy difference of the occupied Eu^{2+} $4f^7$ ground state to the valence and conduction bands in the non-optimized $Sr_2MgSi_2O_7$:Eu^{2+} (CB bottom edge defined using E_g: 7.1 eV) and $SrAl_2O_4$:Eu^{2+} (E_g: 6.6 eV, Eu^{2+} in the Sr1 site).

The position of the occupied Eu^{2+} $4f^7$ ground state of $Sr_2MgSi_2O_7$:Eu^{2+} was identical when calculated with the GGA+U and LDA+U method (Fig. 17). This indicated that both these methods are able to describe the strongly correlated 4f electrons of Eu^{2+} with sufficient accuracy. The agreement between the calculated and experimental E_g values was better with the GGA+U (6.7 eV, *cf.* previous section) than with the LDA+U method (6.4 eV). The GGA(+U) method was thus used instead of LDA(+U) in further calculations.
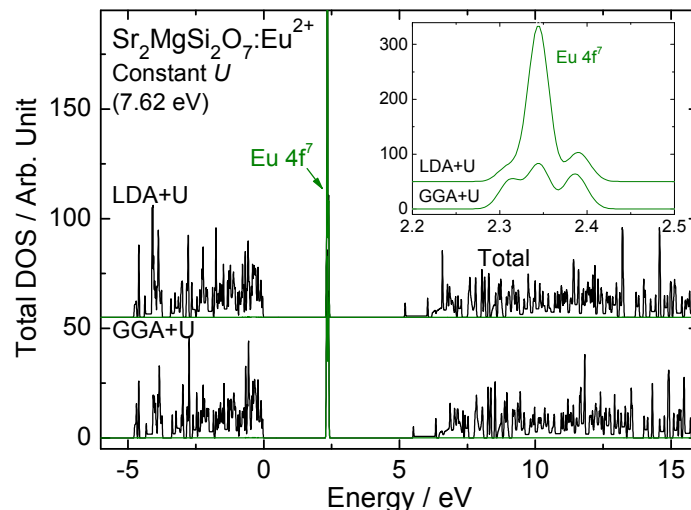
Figure 17. Calculated (GGA+U and LDA+U methods, U: 7.62 eV) density of states of the non-optimized $Sr_2MgSi_2O_7$:Eu^{2+}.

The effect of the structure optimization and the introduction of the spin-orbit coupling in the calculation of the Eu^{2+} doped $Sr_2MgSi_2O_7$ material was studied [III]. The Eu^{2+} $4f^7$ $^8S_{7/2}$ ground state is located only 0.15 eV higher in the optimized than the non-optimized structure (Fig. 18). Inclusion of the spin-orbit coupling leads to the broadening and splitting of the occupied Eu^{2+} $4f^7$ ground state. However, neither the general structure of the valence and conduction bands nor the band gap energy is changed. The width of the $4f^7$ $^8S_{7/2}$ ground state is 0.7 and 0.2 eV with and without spin-orbit coupling, respectively. This is not in agreement with experimental results since the splitting of the Eu^{2+} $4f^7$ ground state ($^8S_{7/2}$) is almost negligible (less than 1 cm^{-1} (0.1 meV)). The reason for such a strong broadening and splitting given by the DFT calculations remains presently unclear. The unoccupied (minority spin) Eu^{2+} $4f^7$ states rise high into the conduction band and are broadened due to the hybridization with the conduction band states (Fig. 15). The influence of spin-orbit coupling is thus not so pronounced for the unoccupied states.
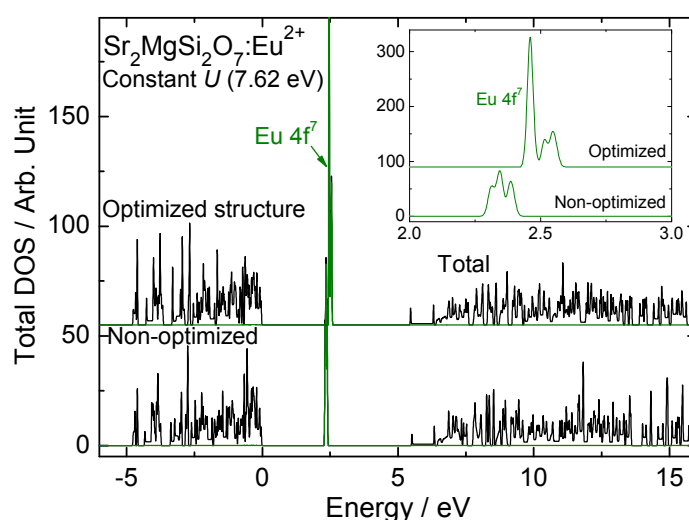
Figure 18. Calculated (GGA+U method, U: 7.62 eV) density of states of the non-optimized and optimized $Sr_2MgSi_2O_7$:Eu^{2+}.

The discrete unoccupied state is found at the same energy as for the non-doped material (*cf.* section 4.4.2) with the introduction of the Eu^{2+} ion. Such electron traps may help to explain the persistent luminescence observed from the disilicate and aluminate materials even without the R^{3+} co-doping. The luminescence spectrum of $SrAl_2O_4$:Eu^{2+} due to the Eu^{2+} $4f^65d^1(^2D)\rightarrow4f^7(^8S_{7/2})$ transitions consists of two bands centered at 445 and 520 nm (2.79 and 2.38 eV, respectively) at low temperature (20 K) [193, Fig. 1]. Only one band at 520 nm is observed at RT, however, suggesting thermal quenching of the high energy emission. The energy of these bands depends on the Eu^{2+} $4f^7$ and $4f^65d^1$ ground state energies. First, the effect of the $4f^7$ energy was studied. According to the calculated $SrAl_2O_4$:Eu^{2+} [IV], the $4f^7$ ground state at the Sr2 site was found at a slightly higher energy ($\Delta E_{calc}(4f^n, Sr2/Sr1)$: 0.09 eV) than at Sr1 using a constant U value (Fig. 19).
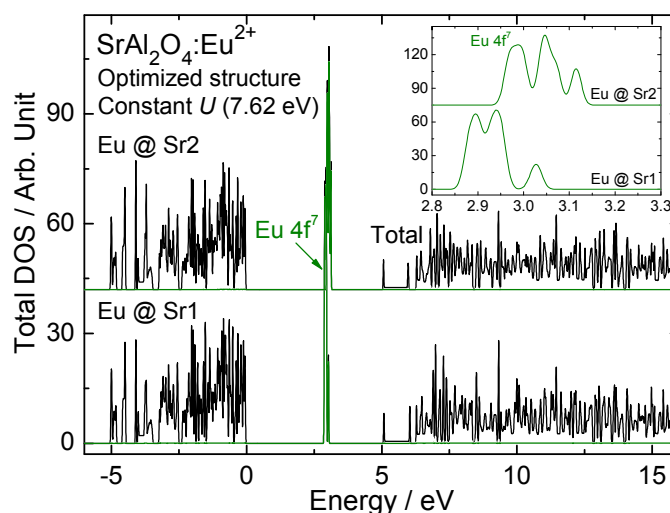
Figure 19. Calculated (GGA+U method, U: 7.62 eV) density of states of the optimized $SrAl_2O_4$ with Eu^{2+} in the Sr1 and Sr2 sites.

A calculated difference in U (ΔU_{calc}(Sr2/Sr1): 0.31 eV) which corresponds to $\Delta E_{calc}(4f^n$, Sr2/Sr1) was obtained using the linear dependence of the $4f^7$ energy on U (Fig. 16). Different Eu-O distances for the two Sr sites (average difference Δr_{calc}(Sr2/Sr1): 0.008 Å) were found (IV, Table 1). The ratio Δr_{calc}(Sr2/Sr1)/ΔU_{calc}(Sr2/Sr1): 0.026 Å/eV was chosen to describe the dependence of the Coulomb repulsion strength U on the changes in the electron repulsion with changing Eu-O distances. However, this dependency is not necessarily linear.

The energy difference of 0.41 eV between the two luminescence bands corresponds to ΔU_{calc}(Sr2/Sr1) of 1.39 eV (Fig. 14). Using the ratio above, this U difference is created by a difference of 0.036 Å (ca. 1.4 % relative to the original distance) in the Eu-O distances of the two sites. This difference should thus be enough to shift the Eu^{2+} $4f^7$ ground state by 0.41 eV and it is similar to the changes obtained due to structural optimization. These results indicate that the two bands may originate also from the two Sr sites. However, the Eu^{2+} $4f^6 5d^1$ ground state has to be determined to solve the origin of the luminescence bands (cf. section 4.4.5.).

4.4.4. $4f^6 5d^1$ Ground State of Eu^{2+} in $Sr_2MgSi_2O_7$

The DFT calculations provide important theoretical evidence on the position of the Eu^{2+} $4f^6 5d^1$ ground state. The $4f^6 5d^1$ electron configuration (the ^2D level) should be split into five components by the crystal field of low symmetry (C_1 in $Sr_2MgSi_2O_7$) [194]. The total energy span of the $4f^6 5d^1$ levels is close to 25 000 cm^{-1} (3.1 eV) in oxides as in $Sr_2MgSi_2O_7$. Therefore, some of these levels are located within CB. The calculated states within and close to the bottom of CB of $Sr_2MgSi_2O_7$:Eu^{2+} possess significant Eu^{2+} 5d character which provides theoretical verification for the empirical model of persistent luminescence [16]. The lowest state with distinct Eu^{2+} 5d character is located at ca. 0.8 eV below CB (Fig. 20). These results confirm that the $4f^6 5d^1$ states are located – at least partly – in CB and the escape of the excited electrons to CB is possible also with relatively low excitation energies. Therefore, an efficient excitation is obtained even without UV radiation. The radiation is thus stored to charge the persistent luminescence.
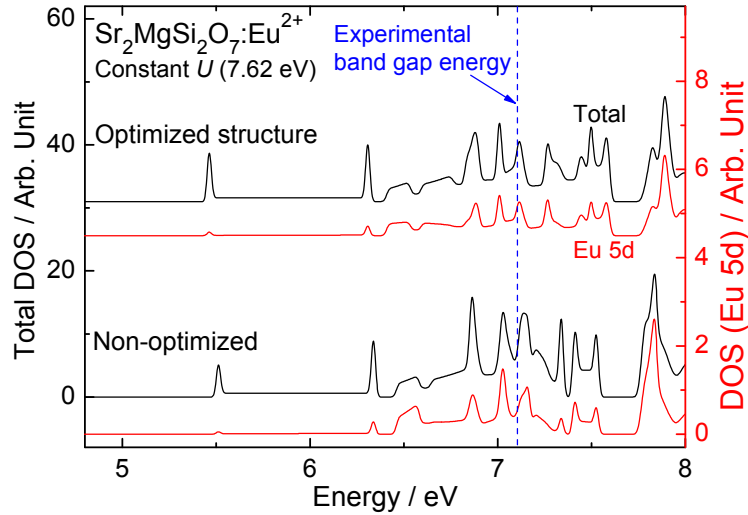
Figure 20. Calculated (GGA+U method, U: 7.62 eV) density of the Eu^{2+} $4f^6 5d^1$ states of the non-optimized and optimized $Sr_2MgSi_2O_7:Eu^{2+}$.

The energy difference between the $4f^7$ and the $4f^6 5d^1$ ground stated can be approximately deduced from experiments when the energy of the luminescence band due to the $4f^6 5d^1(^2D) \rightarrow 4f^7(^8S_{7/2})$ transition of Eu^{2+} is known. Such luminescence band in the $Sr_2MgSi_2O_7:Eu^{2+}$ material is observed at 470 nm (2.6 eV) [195]. The corresponding calculated $4f^6 5d^1$-$4f^7$ energy difference is 3.8 eV (U: 7.62 eV) with the optimized structure. This should be considered as an approximated value since the fixing of the 5d occupation was not feasible with the DFT calculations. Therefore, the states with a distinct 5d character were used to estimate the $4f^6 5d^1$ energies. In addition, the experimental value underestimates the energy difference due to the relaxation of $4f^7$ after the emission which results in a better agreement. The exact amount of especially the 4f relaxation energy depends on the appropriate host lattice and cannot be calculated or obtained from the experimental data but can be estimated to less than 5 000 cm^{-1} (0.62 eV).

4.4.5. $4f^6 5d^1$ Ground State of Eu^{2+} in $SrAl_2O_4$

The Eu^{2+} $4f^6 5d^1$ ground state has to be studied in detail to study the origin of the two luminescence bands of $SrAl_2O_4:Eu^{2+}$ (*cf.* section 4.4.3.) at low temperature. Luminescence is usually observed only from the Eu^{2+} $4f^6 5d^1$ ground state since the higher states are easily relaxed to the $4f^6 5d^1$ ground state located below the bottom of CB. On the other hand, luminescence from a higher Tm^{2+} $4f^{12}5d^1$ state has been reported [196,197] and it is not excluded that Eu^{2+} may exhibit the same kind of unusual low temperature luminescence due to the absence of high energy lattice vibrations. The calculated $4f^6 5d^1$ DOS of $SrAl_2O_4:Eu^{2+}$ (Fig. 21) shows more than one $4f^6 5d^1$ state below CB which is a requirement essential for luminescence to be observed from a higher 5d state [IV].
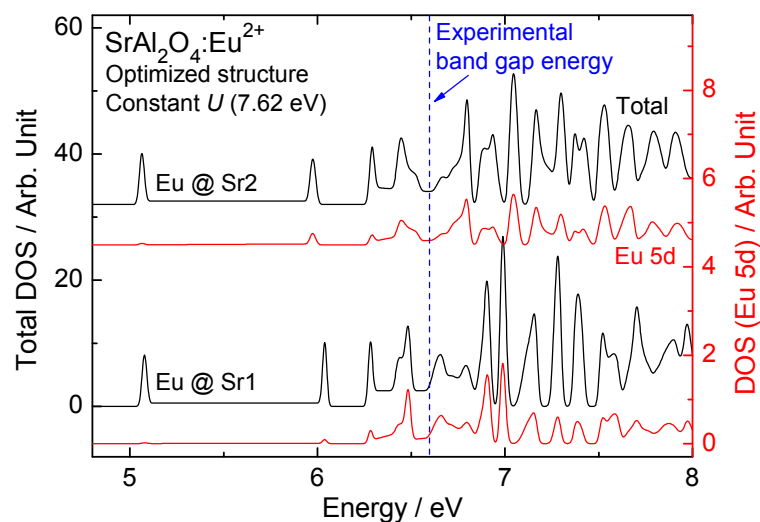
Figure 21. Calculated (GGA+U method, U: 7.62 eV) density of the Eu^{2+} $4f^6 5d^1$ states of the optimized $SrAl_2O_4:Eu^{2+}$ with Eu^{2+} in the Sr1 and Sr2 sites.

Furthermore, the $4f^6 5d^1$ DOS located slightly (0.1-0.2 eV) below the bottom of CB is significantly higher than the one located at *ca.* 0.6 eV below CB (Fig. 21) [IV]. The energy difference of 0.4-0.5 eV between these states corresponds very well to the experimentally observed energy difference of 0.41 eV between the luminescence bands. Luminescence may therefore be observed from both the ground (corresponding to λ_{em}: 520 nm) and a higher (445 nm) $4f^6 5d^1$ state at low temperature resulting in two bands (Fig. 22, right). As discussed above (*cf.* section 4.4.3.), these bands might also be due to Eu^{2+} luminescence from the two Sr sites. In this case, an efficient energy transfer (ET) between them may take place (Fig. 22, left).
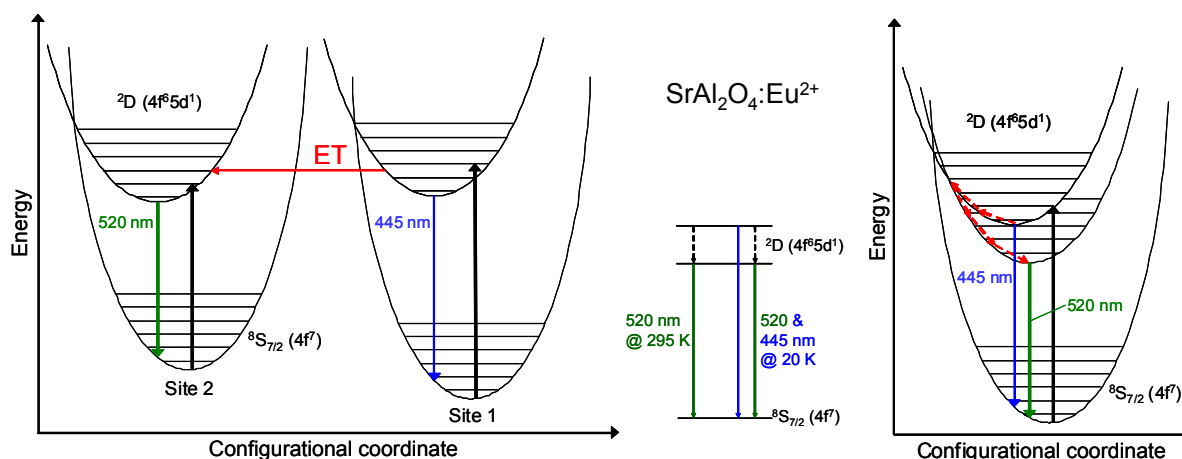
Figure 22. Luminescence processes of $SrAl_2O_4:Eu^{2+}$ at 20 and 295 K, luminescence from two sites (left) or from higher $4f^6 5d^1$ states of one site (right).

4.4.6. $4f^n$ Ground State of $R^{2+/3+}$

The $4f^n$ and $4f^{n-1}5d^1$ ground state energies of the R^{2+} (R_{Sr}^x) and R^{3+} ($R_{Sr}^\bullet$) ions in the band structure of $Sr_2MgSi_2O_7$ have been estimated using the empirical model [16,17]. However, the $4f^n$ ground state positions obtained by this model include a systematic error which is assumed to be of the order of 0.5 eV [15] (*cf.* section 1.). Therefore, the DFT calculations provide a very good alternative to determine the $R^{2+/3+}$ energies in a solid host. In contrast, the R^{3+} (in very limited cases also R^{2+}) $4f^n$ ground and excited states' properties (*e.g.* energy) can be calculated to very high accuracy using semiempirical simulation techniques [*e.g.* 198]. The use of the density functional theory (DFT) *ab initio* methods on the rare earth systems has been restricted to only a few R^{3+} (R: Sm, Eu, Er, Tm) doped in simple hosts as *e.g.* AlN [7], SiC [8], and GaN [9] (Table 3, section 2.3.).

The present calculations indicate that, as a result of the $R^{2+/3+}$ doping, additional $4f^n$ and $4f^{n-1}5d^1$ states were introduced in the $Sr_2MgSi_2O_7$ band structure (Fig. 23). Especially, the band structure close to the bottom of CB was modified (*cf.* section 4.4.7.). The characteristic trend for the R^{3+} (also R^{2+}) $4f^n$ ground state energies is understood based on the differences in *e.g.* the ionization energies. The energy is the highest when the 4f shell is filled (n: 14) or half filled (n: 7) due to the electron spin pairing and lowest for n: 1 and 8 [199,200]. According to the empirical model, this trend is important since it is rather independent of the host lattice [15]. All the R^{3+} (R^{2+}) $4f^n$ ground states can thus be located in the host band structure if the $4f^n$ ground state energy of one R^{3+} (R^{2+}) ion is known.
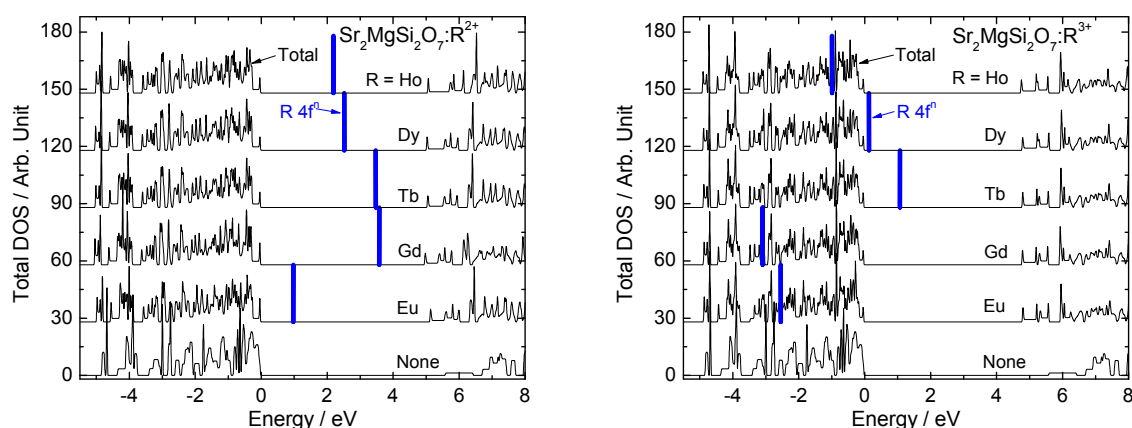
Figure 23. Calculated (GGA method) band structure of selected $Sr_2MgSi_2O_7$:R (R^{2+}: left; R^{3+}: right; R: Eu-Ho).

The calculated trend in the R^{3+} $4f^n$ ground states matches well with the characteristic empirical trend (Figs. 23 and 24). Also, the $4f^n$ ground state energies relative to VB agree well with the values derived from the empirical model [15,17] as illustrated by *e.g.* the calculated Ce^{3+} $4f^1$ ground state locating at 2.9 eV above VB (empirical model: 3.6 eV). The minor differences between the calculated and empirical trend and energy for the R^{3+} $4f^n$ ground states are probably due to the insufficient handling of the electron spin pairing by the GGA method and to the experimental inaccuracies. The DFT results suggest that at least Ce^{3+}, Pr^{3+} and Tb^{3+} are able to act as hole traps in $Sr_2MgSi_2O_7$ since the energy difference between the top of VB and the R^{3+} $4f^n$ ground state determines this

ability. This information is, of course, given by the conventional wisdom since only these R^{3+} ions can achieve easily the stable R^{IV} oxidation state. Nevertheless, the hole traps are not relevant for the persistent luminescence mechanism of the Eu^{2+} doped materials since the electrons act as the charge carriers in *e.g.* $Sr_2MgSi_2O_7:Eu^{2+}$ (*cf.* section 4.4.3.).
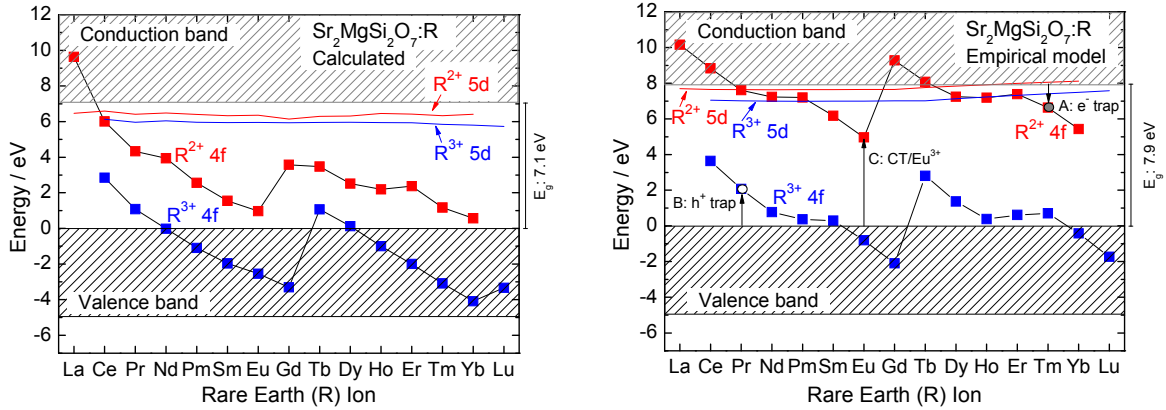
Figure 24. Calculated (left, GGA method) and experimental (right) $R^{2+/3+}$ (R: La-Lu) $4f^n$ and $4f^{n-1}5d^1$ ground state energies in $Sr_2MgSi_2O_7$.

The experimental trend in the R^{2+} $4f^n$ ground state energies is reproduced well for the both ends of the R^{2+} series (R^{2+}: Ce^{2+}-Eu^{2+} and Tb^{2+}-Yb^{2+}) (Fig. 24). However, a significant difference was found between the calculated and empirical trends when the entire R^{2+} series is considered. The energy difference between the La^{2+} and Yb^{2+} $4f^n$ ground state energies is 9.1 (calculated) and 4.7 eV (empirical). The DFT calculations may thus indicate that the trend in the R^{2+} ground state positions is not entirely independent of the host lattice. The accuracy of the prediction of the R^{2+} state positions is extremely important in the Eu^{2+},R^{3+} doped persistent luminescence materials since the ability of the R^{3+} co-dopant to act as an electron trap can be estimated from the energy difference between the bottom of CB and the R^{2+} $4f^n$ ground state (process A shown for Tm, hole trapping process B for Pr, Fig. 24) [15].

The La^{2+} $4f^1$ ground state energy obtained from the empirical model (3.1 eV within CB) is quite accurately reproduced by the DFT calculations (2.5 eV) (Fig. 24). The calculated $4f^n$ ground state energies of other R^{2+} (Ce^{2+}-Yb^{2+}) ions in $Sr_2MgSi_2O_7$ are located closer to VB than estimated by the empirical model. The calculated $4f^n$ energy difference between the R^{2+} and R^{3+} ions corresponding to the electron affinity for the same element ($\Delta E(4f^n, R^{2+/3+})$: 2.4-4.7 eV) is underestimated from the values (5.2-6.8 eV for $Sr_2MgSi_2O_7$) obtained using the empirical model [15,17]. It would be very important to study further whether or not the variation of the energy difference $\Delta E(4f^n, R^{2+/3+})$ on the inorganic host material is small enough for this parameter to be considered as host independent. If this is indeed the case, *all* the R^{2+} and R^{3+} $4f^n$ ground states can be obtained from the known trends and their energy differences using only a single experimental point (*e.g.* charge transfer of Eu^{3+}).

The R^{3+} charge transfer (CT) energies can be derived from the energy difference between VB and the $4f^n$ ground state position of the R^{2+} ion (process C, Fig. 24). The calculated CT energies (*e.g.* Eu^{3+}: 1.0 (calculated), 5.0 eV (experimental)) are largely underestimated due to the R^{2+} $4f^n$

ground states locating too low relative to CB. The reason(s) for this discrepancy remains unclear. Preliminary studies using the GGA+U method for selected $R^{2+/3+}$ (*e.g.* Gd^{3+}) to better describe the strongly correlated 4f electrons have already been carried out.

4.4.7. $4f^{n-1}5d^1$ Ground State of $R^{2+/3+}$

According to the empirical model [15], the $4f^{n-1}5d^1$ ground state for the R^{2+} (also R^{3+}) ions are found at approximately the same energy irrespective of the rare earth. This host independent trend is well reproduced by the calculations (Figs. 24 and 25). Moreover, the $4f^{n-1}5d^1$ ground states are located at *ca.* 0.7 (R^{2+}) and 1.2 eV (R^{3+}) below the bottom of CB of $Sr_2MgSi_2O_7$ which is in good agreement with the empirical model (*ca.* 0.2 and 0.9 eV below CB, respectively). The energy difference between the R^{2+} and R^{3+} series ($\Delta E(4f^{n-1}5d^1, R^{2+/3+})$: 0.5 eV) is only slightly lower than the empirical value (0.7 eV). The empirical model predicts a slight increase of *ca.* 0.5 eV in the $4f^{n-1}5d^1$ ground state energy when moving to the heavier rare earths in the $R^{2+/3+}$ series (Fig. 25). This increase, however, is not reproduced by the DFT calculations.
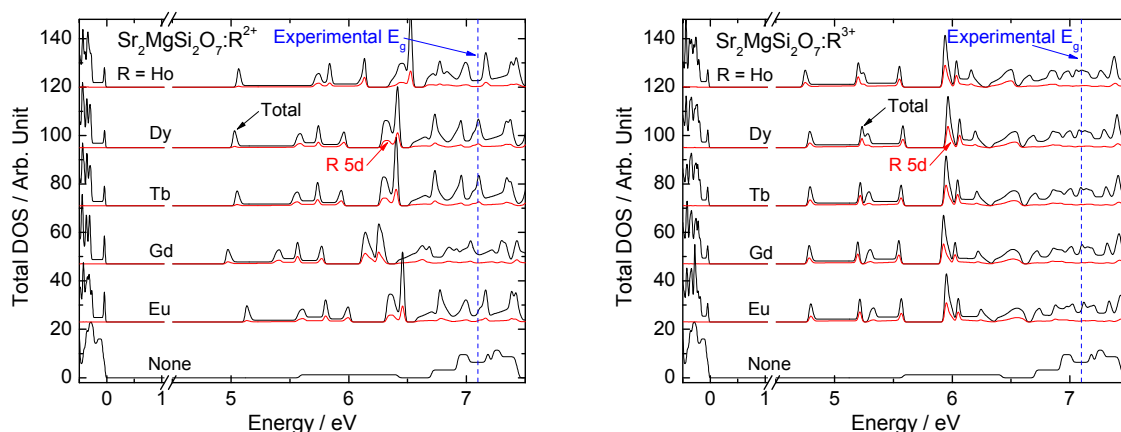
Figure 25. Calculated (GGA) $4f^{n-1}5d^1$ states for selected $Sr_2MgSi_2O_7$:R (R^{2+}: left; R^{3+}: right; R: Eu-Ho).

The doping with $R^{2+/3+}$ results in the creation of some almost discrete unoccupied states without distinct 5d character just below CB (Fig. 25). These states may indicate the creation of shallow electron traps which increases the persistent luminescence intensity and/or duration. These results suggest that the role of the (co-)doping $R^{2+/3+}$ ions in the persistent luminescence materials may be even more versatile than reported earlier, in addition to adding new defects and/or modifying the depths of the existing ones.

The calculated $R^{2+/3+}$ $4f^n$ and $4f^{n-1}5d^1$ ground states in the $Sr_2MgSi_2O_7$ band structure (Figs. 24 and 25), in combination with the wide band gap of $Sr_2MgSi_2O_7$ (*cf.* section 4.4.1.), confirm the role of electrons as the charge carriers responsible for persistent luminescence in the materials doped not only with Eu^{2+} but also with Ce^{3+} and Tb^{3+} since the excitation energy raises the electron close to the bottom of or in CB. The electron trapping also takes place close to CB as the electron traps have traditionally been assumed to do. In addition, the energy cost of releasing a hole (h^+) from Eu^{2+} in its excited $4f^65d^1$ state has been shown to be much too high for the hole to be considered as a possible effective charge carrier in these systems [201].

4.4.8. Isolated Defects

The effect of the isolated vacancies on the electronic structure of the $Sr_2MgSi_2O_7$ and $SrAl_2O_4$ materials was studied next [V,VII]. The introduction of one strontium vacancy in the normal unit cell of $Sr_2MgSi_2O_7$ and $SrAl_2O_4$ results in an increase (*ca.* 0.4 eV) in the E_g value (Figs. 26 and 27), possibly due to the predominantly Sr character of the bottom of CB (*cf.* section 4.4.1.). A discrete V_{Sr}'' state is located at *ca.* 1 eV below the bottom of CB possibly acting as a shallow electron trap in $Sr_2MgSi_2O_7$ and $SrAl_2O_4$. The number of the V_{Sr}'' traps is radically increased due to the charge compensation when R^{3+} replaces Sr^{2+}. Some R^{3+} have been observed to greatly enhance the persistent luminescence while some others have a detrimental effect [*e.g.* 14]. In addition to the introduction of new electron traps with the R^{3+} co-doping, the modification of the present ones is possible. The introduction of V_{Si}'''' in $Sr_2MgSi_2O_7$ creates some nearly continuous density of unoccupied states extending to *ca.* 2 eV below the bottom of CB, whereas V_{Mg}'' does not change the electronic structure close to CB. A deep electron trap at 3.8 eV below CB is created by V_{Al}''' in $SrAl_2O_4$ (Fig. 27).
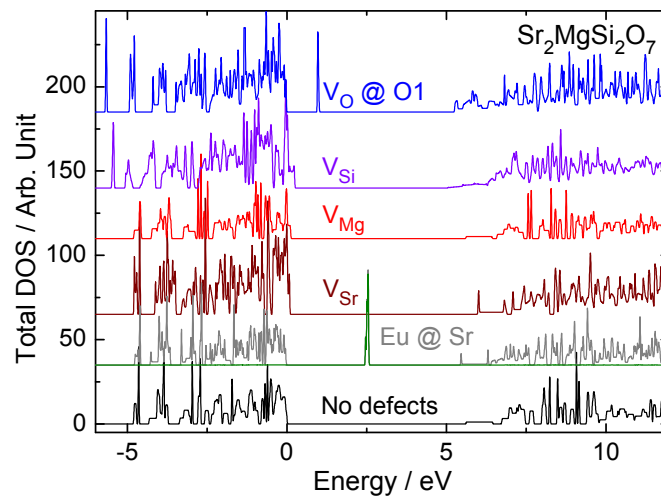
Figure 26. Calculated (GGA method) density of states of the optimized $Sr_2MgSi_2O_7$ with isolated defects.
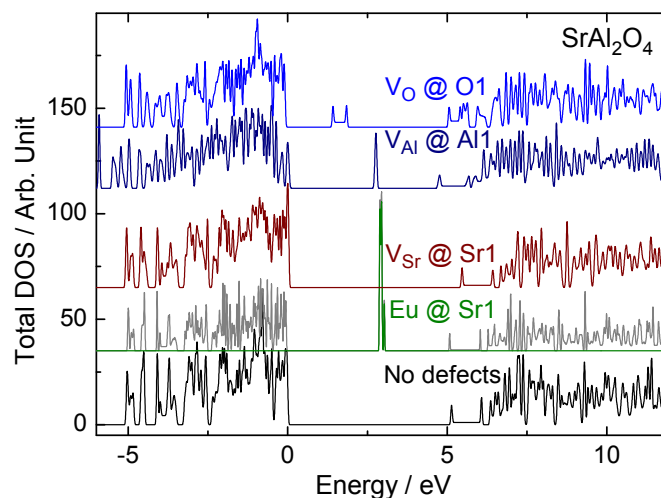
Figure 27. Calculated (GGA method) density of states of the optimized $SrAl_2O_4$ with strontium, aluminium and oxygen vacancy in the Sr1, Al1 and O1 sites, respectively.

The introduction of an isolated oxygen vacancy in $Sr_2MgSi_2O_7$ and $SrAl_2O_4$ results in the creation of substantial density of unoccupied states close to the bottom of CB (Figs. 26-28) [V,VII]. These $V_O^{\bullet\bullet}$ states indicate the presence of a high number of shallow electron traps. The $V_O^{\bullet\bullet}$ states corresponding to the deepest traps which may still be available for persistent luminescence are located at *ca.* 1.8 eV below CB. However, the very shallow electron traps created by $V_O^{\bullet\bullet}$ closest to CB can be bleached with a significantly low amount of thermal energy. The experimentally observed rapid initial weakening of persistent luminescence [202] can be explained by the easy release of electrons from the traps closest to the conduction band. The experimental verification of the very shallow electron traps would require *e.g.* the thermoluminescence studies to be carried out at low temperatures. The introduction of $V_O^{\bullet\bullet}$ in the O1 site creates slightly (*ca.* 0.1 eV) deeper traps compared to the O2 and O3 site (Fig. 28). The differences between the oxygen sites were reflected also by the structure optimization (*cf.* section 4.3.2.).
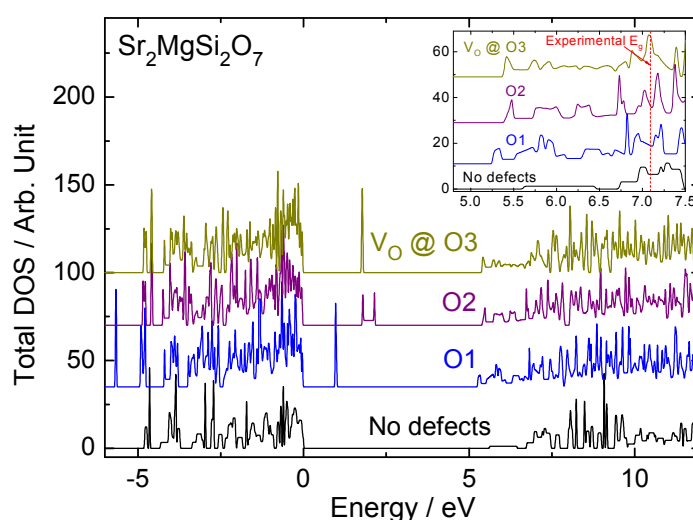
Figure 28. Calculated (GGA method) density of states of the optimized $Sr_2MgSi_2O_7$ with oxygen vacancy in the different oxygen sites.

Additional oxygen vacancy states are located at 5-6 eV below CB indicating the presence of deep electron traps in the $Sr_2MgSi_2O_7$ and $SrAl_2O_4$ hosts (Figs. 26-28) [V,VII]. However, electrons in these deep traps are not available for the persistent luminescence due to the high amount of energy required to bleach the traps. The effect of the defect concentration on the calculated trap structure of $Sr_2MgSi_2O_7$ was studied, as well. No significant changes were found in the electronic structure whether the high (normal unit cell: 7 %) or low (2x2x2 supercell: 1 %) defect concentration was used for $V_O^{\bullet\bullet}$ in $Sr_2MgSi_2O_7$ (Fig. 29). The deepest trap still available for persistent luminescence is shifted (*ca.* 0.3 eV towards VB) with the lowering defect concentration. The change from normal cell to the supercell had no effect on the host band structure.
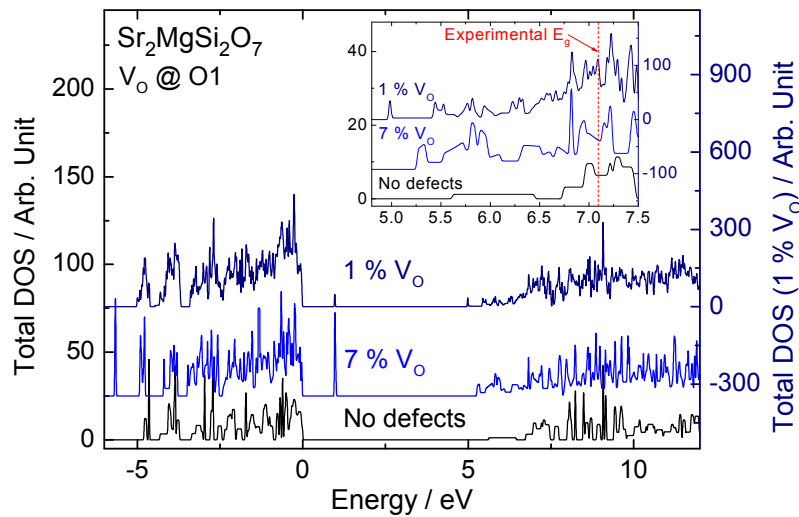
Figure 29. Calculated (GGA method) density of states of the optimized $Sr_2MgSi_2O_7$ with oxygen vacancy in the O1 site in the normal unit cell (7 % defect concentration) and the 2x2x2 supercell (1 %).

Strontium, magnesium, silicon and aluminium vacancies create traps slightly (*ca.* 0.1, 0.1, 0.2, and 0.1 eV, respectively) above the top of the valence band of $Sr_2MgSi_2O_7$ and $SrAl_2O_4$, as well (Figs. 26 and 27) [V,VII]. These states indicate the presence of shallow hole traps in the material, though a very efficient hole transfer between these shallow hole traps and VB is expected at room temperature. The almost negligible difference between the electronic structures of V_{Sr}'' located in the Sr1 or Sr2 site of $SrAl_2O_4$ highlights the similarity of these two sites (Fig. 30). No significant role for the hole traps in the persistent luminescence of the Eu^{2+} doped materials is expected, though.
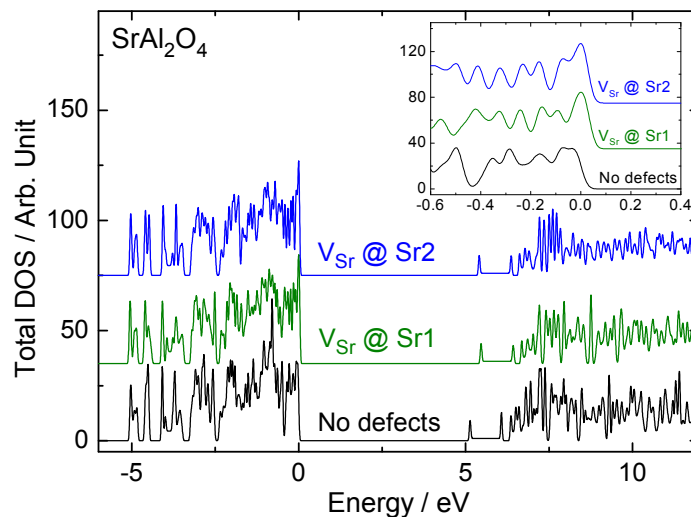
Figure 30. Calculated (GGA method) density of states of the optimized $SrAl_2O_4$ with strontium vacancy in the Sr1 and Sr2 sites.

4.4.9. Defect Aggregates

The interactions between the defects need to be accounted for in the DFT calculations since even very short distances between them may occur rather frequently in the material. This is due to the relatively high total concentration of the defects (due to high charging capasity of the materials) as well as the creation of the defect pairs and other defect aggregates induced by the charge compensation. Electrostatic interactions favor aggregation, too. The modification of the vacancy induced traps due to the presence of the Eu^{2+} luminescent centre as well as due to the co-doping R^{3+} ion is expected to have an important effect on the persistent luminescence efficiency. The detailed analysis of the thermoluminescence glow curves has indicated such features in the trap structure [14,V].

Selected defect pairs ($Eu_{Sr}^x + V_{Sr}''$, $Eu_{Sr}^x + V_O^{\bullet\bullet}$ and $V_{Sr}'' + V_O^{\bullet\bullet}$) were used to study the effect of the interactions between the defects on the electronic structure of $Sr_2MgSi_2O_7$ with the DFT calculations [VII]. The strontium vacancy was introduced at the closest possible distance (4.22 Å) from the Eu^{2+} ion, whereas the oxygen vacancy and Eu^{2+} were introduced at different distances in the $Sr_2MgSi_2O_7$ lattice. To facilitate the task, the calculated (GGA method) energy of the Eu^{2+} $4f^7$ ground state at 2.5 eV above the top of VB for the $Eu_{Sr}^x + V_{Sr}''$ pair is similar to the isolated Eu^{2+} ground state position calculated using the GGA+U method (*cf.* section 3.5.).

The $Eu_{Sr}^x + V_{Sr}''$ and $Eu_{Sr}^x + V_O^{\bullet\bullet}$ pairs create an almost continuous density of unoccupied states extending to *ca.* 2 eV below the bottom of the conduction band (Fig. 31) [VII]. This indicates that the interactions between the Eu^{2+} luminescent centre and V_{Sr}'' as well as $V_O^{\bullet\bullet}$ indeed modify the electron traps created by the isolated defects. Therefore, they may have a significant effect on the energy storage efficiency as well as the intensity and duration of persistent luminescence. The density of the unoccupied states created by a $Eu_{Sr}^x + V_O^{\bullet\bullet}$ pair is higher than the one created by $Eu_{Sr}^x + V_{Sr}''$. The $V_{Sr}'' + V_O^{\bullet\bullet}$ pair creates an even higher density of unoccupied states close to the bottom of CB than the $Eu_{Sr}^x + V_{Sr}''$ and $Eu_{Sr}^x + V_O^{\bullet\bullet}$ pairs. In addition, several states are created above the top of VB significantly decreasing the band gap which effect cannot be explained at present.
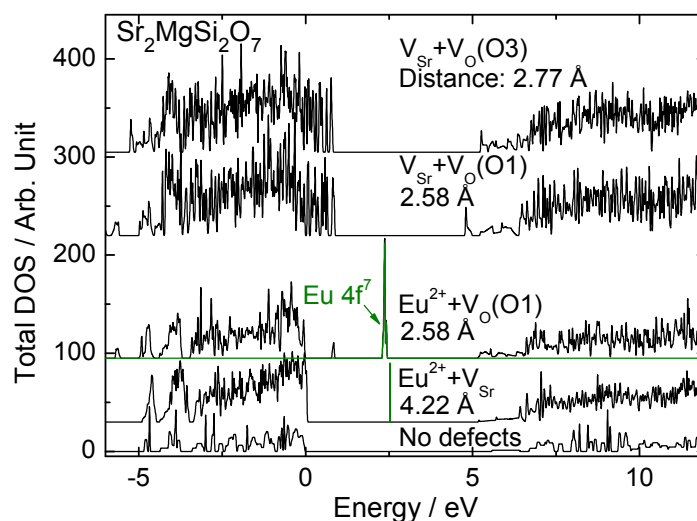
Figure 31. Calculated (GGA and GGA+U methods, *U*: 7.62 eV) density of states of the optimized $Sr_2MgSi_2O_7$ with defect pairs ($V_{Sr}'' + V_O^{\bullet\bullet}$ and $Eu_{Sr}^x + V_O^{\bullet\bullet}$: 1x1x3 supercell, $Eu_{Sr}^x + V_{Sr}''$: 1x1x2 supercell).

The interaction between the Eu^{2+} ion and $V_O^{\bullet\bullet}$ lowers the energies of both the Eu^{2+} $4f^7$ ground state and the deep $V_O^{\bullet\bullet}$ state (Fig. 32, see also Fig. 26) [VII]. A decrease of approximately 0.2 eV when Eu_{Sr}^x and $V_O^{\bullet\bullet}$ are located as the nearest neighbors (distance: 2.6-2.8 Å) when compared to the position of the corresponding isolated defects. A less significant decrease (*ca.* 0.1 eV) is found when the distance between Eu^{2+} and $V_O^{\bullet\bullet}$ is increased (5 to 7 Å). However, the modified trap structure created close to the bottom of CB by the $Eu_{Sr}^x + V_O^{\bullet\bullet}$ pair remains similar despite the distance between the defects is changed. These results confirm that the interaction between Eu^{2+} and $V_O^{\bullet\bullet}$ exists at relatively long distances in the $Sr_2MgSi_2O_7$ host. The interactions at even longer distances between Eu^{2+} and $V_O^{\bullet\bullet}$ need still to be studied using very large supercell calculations.
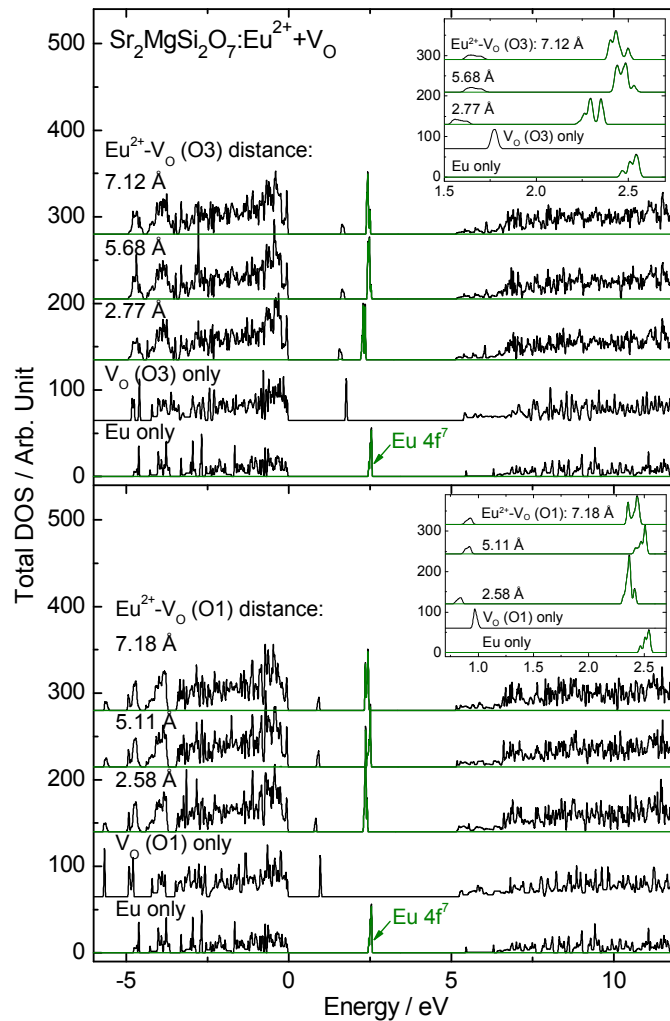
Figure 32. Calculated (GGA+U method, *U*: 7.62 eV) density of states of the optimized $Sr_2MgSi_2O_7$ with Eu^{2+} located at different distances from $V_O^{\bullet\bullet}$ in the O1 and O3 sites in the 1x1x3 supercell.

The electron density originally bonding the Eu^{2+} and O^{2-} ions moves towards the Eu^{2+} centre when this O^{2-} ion is replaced by a vacancy [VII]. In addition, the Eu-O distances of the remaining O^{2-} ions surrounding the Eu^{2+} centre are decreased due to the introduction of $V_O^{\bullet\bullet}$ (Table 7) as an indication of reduced ligand repulsion. The Eu^{2+} $4f^7$ ground state shifts to a lower energy due to the increased Eu^{2+} 4f electron repulsion when $V_O^{\bullet\bullet}$ is introduced as the nearest neighbor of Eu^{2+} (Fig. 32). This

effect is similar to the shift of the $4f^7$ ground state towards the valence band with increasing Coulomb repulsion strength (Hubbard parameter U, $cf.$ section 4.4.3.). The increase in the electron repulsion at the Eu^{2+} centre as well as the decrease in the Eu-O distances at the centre is less significant when $V_O^{\bullet\bullet}$ is located at longer distances from Eu^{2+}. This results in a smaller shift in the $4f^7$ ground state position.

4.5. Thermoluminescence

Thermoluminescence (TL) provides a powerful tool to obtain the experimental trap energy structure of the polycrystalline materials (co-)doped with the rare earth ions. However, the nature of the traps remains mostly unknown. The TL glow curve of $Sr_2MgSi_2O_7$:Eu^{2+} consists of a strong band centered at 85 °C and weak bands at 155 and 215 °C (Fig. 33) [V,VI]. The temperature of the strongest TL band is known to be very suitable for promoting the thermally stimulated ($i.e.$ persistent) luminescence at room temperature. In contrast, the deepest electron trap corresponding to the weak band at above 200 °C is probably too deep for efficient release of trapped electrons to the conduction band at RT. The rather inefficient (and slow) tunneling may be then the only way to empty the deep traps. The electrons in the deep trap may lead to photostimulated luminescence, but they are not usually available for persistent luminescence and its intensity is thus decreased.
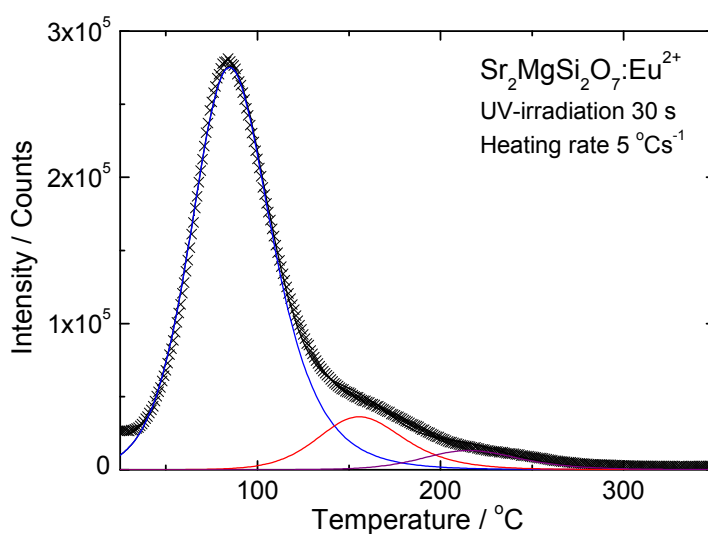
Figure 33. Thermoluminescence (TL) glow curve of $Sr_2MgSi_2O_7$:Eu^{2+} analyzed with the deconvolution method [177,178].

A similar strong TL band at 85 °C along with a weaker band at 105 °C was observed in $Sr_2MgSi_2O_7$:Eu^{2+},Dy^{3+} (Fig. 34) [VI]. The release of the electrons from the deeper trap corresponding to the band at 105 °C is not too fast at RT which is essential for ensuring the long duration of persistent luminescence. However, the release of the electrons remains efficient since the trap is sufficiently close to the conduction band. The requirement of strong luminescence combined with good energy storage at RT due to the shallow and deep traps, respectively, is very well met with the Eu^{2+},Dy^{3+} co-doping. The TL band of $Sr_2MgSi_2O_7$:Eu^{2+},Dy^{3+} at 105 °C was much stronger compared to the high-temperature bands of the Eu^{2+} doped material indicating a significantly stronger persistent

luminescence. However, this may also be due to an artefact due to the short irradiation time favoring the filling of shallow traps only. The weak bands observed at above 150 $^{\circ}$C for the Eu^{2+} doped material do not appear in the glow curve of the Eu^{2+},Dy^{3+} co-doped material probably due to the modification of the defect structure. These bands may also be too weak relative to the strongest band to be observed.
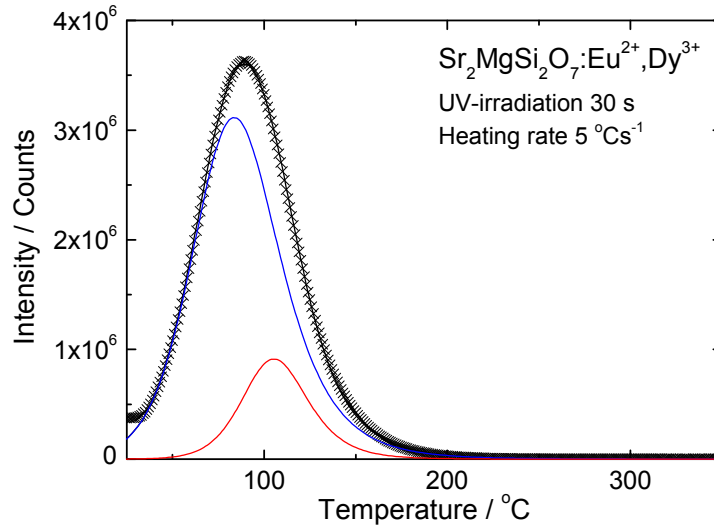
Figure 34. Thermoluminescence (TL) glow curve of Sr$_2$MgSi$_2$O$_7$:Eu^{2+},Dy^{3+} analyzed with the deconvolution method [177,178].

The lattice defects as $V_{Sr}^{''}$ and $V_O^{\bullet\bullet}$ may play a major role in the origin of the TL band of the materials [VI]. Both isolated lattice defects and defect aggregates (*e.g.* Dy$_{Sr}^{\bullet}$ - $V_{Sr}^{''}$ - Dy$_{Sr}^{\bullet}$ and Dy$_{Sr}^{\bullet}$ - $O_i^{''}$) have to be considered as possible electron and hole trapping sites. In addition, the Dy^{3+} co-doping induces the creation of additional defects in the Sr$_2$MgSi$_2$O$_7$ host (*cf.* section 4.2.) thus strongly enhancing the persistent luminescence intensity and duration. The exact interactions within the different defect aggregates present in the doped materials are very challenging to determine using experimental methods.

As a result of the deconvolution procedure, a good agreement between the trap depths and the TL peak temperatures was obtained [V,VI]. The energy of the shallowest trap was 0.70 and 0.63 eV below CB for the Eu^{2+} doped and Eu^{2+},Dy^{3+} co-doped material (Fig. 35), respectively. The width of the energy distribution of the traps is 0.40 and 0.35 eV, respectively. The difference between the experimental trap structure of the Eu^{2+} doped and Eu^{2+},Dy^{3+} co-doped materials suggests smaller differences in the intensity and duration of persistent luminescence than the experimentally observed differences extending up to several orders of magnitude in both aspects [202]. However, significant differences in the observed persistent luminescence properties are expected since the persistent luminescence is controlled by the Boltzmann distribution emphasizing even very small energy difference.
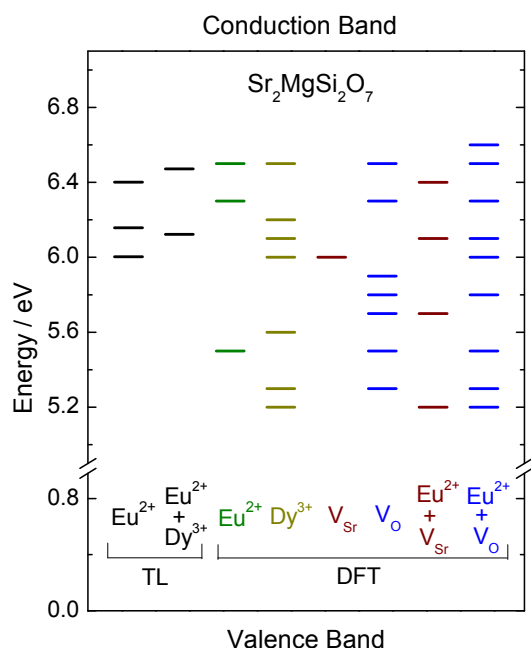
Figure 35. Trap structure obtained from the TL data for $Sr_2MgSi_2O_7:Eu^{2+}(,Dy^{3+})$ and calculated with DFT (GGA(+U) method).

The experimentally derived traps are in the same energy range as the trap structure obtained using the DFT calculations though the calculated energy distribution (*e.g.* Eu^{2+}: 1.0 eV) is broader (Fig. 35). A good agreement was found for the main trap with a depth of 0.6-0.7 eV. Shallower traps were also found using DFT and their presence has been confirmed experimentally since in some cases the R^{3+} co-doping is suppressing the persistent luminescence [*e.g.* 14]. The exact interpretation of the experimental trap depths is difficult since the broad TL bands may include contributions from electron traps created by the different isolated defect and defect aggregate species which are present in the material.

4.6. Conventional Eu^{2+} luminescence

The conventional luminescence spectra of the $Sr_2MgSi_2O_7:Eu^{2+}(,Dy^{3+})$ materials excited to the conduction band by synchrotron radiation (λ_{exc}: 160 nm (7.75 eV)) at 9 K are characterized by a strong band centered at 472 nm (2.63 eV) due to the $4f^65d^1(^2D) \rightarrow 4f^7(^8S_{7/2})$ transition of Eu^{2+} (Fig. 36) [VI]. The emission band is asymmetric probably due to superimposed luminescence band(s) at lower energy originated from the $Sr_3MgSi_2O_8:Eu^{2+}$ (λ_{em}: 482 nm (2.57 eV) [203]) minor impurity phase. The luminescence weakens due to Dy^{3+} co-doping because of the energy stored in the trap(s) created by the isolated lattice defects and/or defect aggregates. The electrons are trapped permanently at 9 K due to insufficient thermal energy available to bleach the traps.
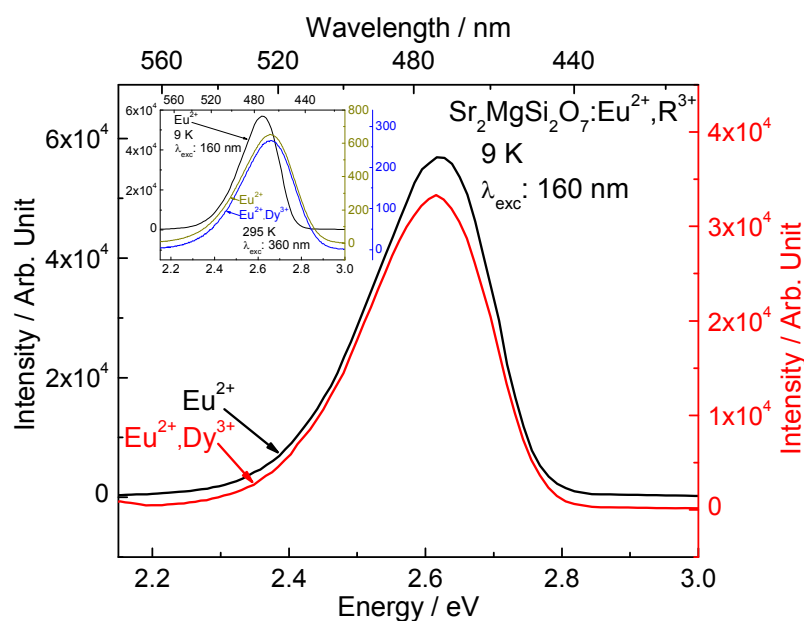
Figure 36. Synchrotron radiation excited (λ_{exc}: 160 nm) emission spectra of the Eu^{2+} doped and Eu^{2+},Dy^{3+} co-doped $Sr_2MgSi_2O_7$ at 9 K (SUPERLUMI, HASYLAB). Inset: comparison to UV excited (λ_{exc}: 360 nm) emission spectra at 295 K.

The UV excited (λ_{exc}: 360 nm (3.44 eV)) luminescence spectra of the $Sr_2MgSi_2O_7$:Eu^{2+}(,Dy^{3+}) materials show a band centered at 466 nm (2.66 eV) at room temperature (Fig. 36, inset) [VI]. The small increase of 0.038 eV in the band energy compared to the synchrotron radiation measurement temperature is due to the effect of the crystal field. The crystal field increases due to the shrinking of the lattice with decreasing temperature. The crystal field splitting of the Eu^{2+} $4f^65d^1$ states becomes thus more pronounced and the $4f^65d^1$ ground state shifts to lower energy decreasing the band energy at low temperature. The luminescence weakened because of co-doping also at RT probably due to (permanent) electron trapping. This indicates an efficient energy storage of $Sr_2MgSi_2O_7$:Eu^{2+},Dy^{3+} even at RT. The thermal energy available at RT does not bleach the electron traps immediately due to the deepening of the traps with the introduction of Dy^{3+}. The decrease in the photoluminescence intensity of $Sr_2MgSi_2O_7$:Eu^{2+},Dy^{3+} is thus compensated by the long duration of the persistent luminescence when the stored energy is released from the traps.

The VUV excitation of $Sr_2MgSi_2O_7$:Eu^{2+}(,Dy^{3+}) results in a transition from VB to CB, whereas the UV-vis excitation corresponds to the direct $4f^7 \rightarrow 4f^65d^1$ excitation of Eu^{2+} (Fig. 37) [VI]. An accurate E_g value is difficult to derive due to the temperature effect and the presence of possible excitonic features at the bottom of the conduction band (*cf.* section 4.4.1.). The spectrum was thus recorded at 9 K to minimize the temperature effect. The Eu^{2+} $4f^7 \rightarrow 4f^65d^1$ transitions appear as four broad bands over the energy range from *ca.* 190 to 330 nm (6.5 to 3.8 eV). In principle, the crystal field splitting of the $4f^65d^1$ configuration (*cf.* section 4.4.4.) should create five main components in the excitation spectrum [194]. The weak band at 200 nm (6.2 eV) probably corresponds to excitation to the highest $4f^65d^1$ state and the excitation to the $4f^65d^1$ ground state is above 330 nm (3.8 eV), the experimental limit of the setup. The remaining part of this configuration, namely $4f^6$, should be visible as a fine

structure composed of seven (^7F_J) sharper bands [204]. However, neither the main components nor the fine structure could be clearly observed due to the strongly overlapping bands.
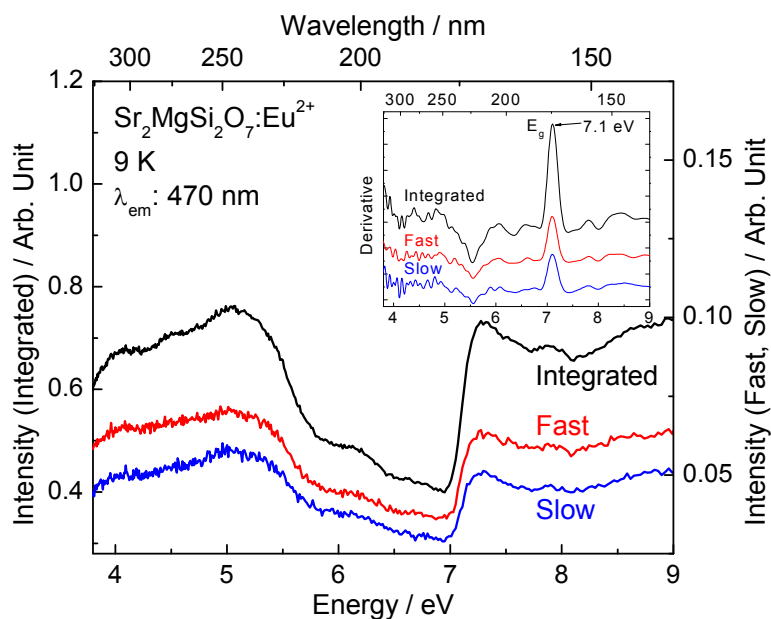
Figure 37. UV-VUV synchrotron radiation excitation spectrum of Eu^{2+} emission (470 nm) from $Sr_2MgSi_2O_7$:Eu^{2+} at 9 K (SUPERLUMI, HASYLAB). Delay: integrated: 2 - 190; fast: 2 - 20 and slow: 170 - 190 ns. Inset: derivative curve of the excitation spectra.

4.7. Persistent Luminescence Mechanism

The position of the Eu^{2+} $4f^7$ ground state close to the conduction band confirms that electrons act as the charge carriers responsible for persistent luminescence in the Eu^{2+} doped materials (*cf.* sections 4.4.3. and 4.4.7.). The persistent luminescence process of the $Sr_2MgSi_2O_7$:Eu^{2+},R^{3+} and $SrAl_2O_4$:Eu^{2+},R^{3+} materials commences with the $4f^7 \rightarrow 4f^6 5d^1$ photoexcitation of Eu^{2+} which is induced by blue light or UV radiation (process 1, Fig. 38). The excited electron can escape directly to CB from a $4f^6 5d^1$ state located within CB (2a). It can also escape from a $4f^6 5d^1$ state below CB with the aid of thermal energy (2b) ensuring a broad excitation of persistent luminescence. The Eu^{2+} ion becomes thus either an excited $(Eu^{3+})^*$ species or an excited $(Eu^{2+}-h^+)^*$ pair. The electron moving quite freely in CB is then captured by traps close to the bottom of CB (3). The temperature controlled gradual transfer of the electrons from the defects acting as shallow electron traps back to CB takes place at room (or, in fact, at any other desired) temperature (4). The release of the trapped electrons is followed by their migration (or retrapping) to the luminescent centre through CB for the recombination and emission of visible light (5). The retrapping processes may prolong the duration of persistent luminescence or lead to energy losses. Direct tunnelling of electrons between the trapping site and the luminescent centre may also take place instead of the migration of electrons through CB.
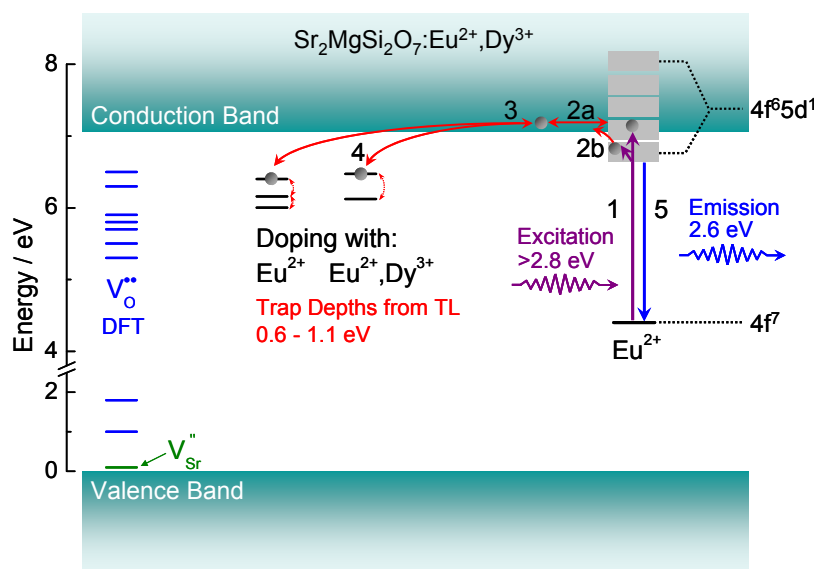
Figure 38. Persistent luminescence mechanism of $Sr_2MgSi_2O_7$:Eu^{2+},Dy^{3+}. Processes indicated with arrows are explained in the text.

The origin of the electron traps can be *e.g.* the R^{3+} co-doping (ion), a vacancy or even defect aggregates. The R^{3+} co-dopant may trap an electron from the conduction band thus creating the R^{2+} species [16]. In addition, efficient trapping of electrons by the oxygen vacancies is expected. The creation of F^+ (or F) color centres has indeed been verified by EPR measurements [205]. The depth of the electron traps is essential since too shallow traps are bleached quickly at RT thus reducing the duration of persistent luminescence. In addition, a high number of the traps is required to ensure efficient energy storage.

5. CONCLUSIONS

The crystal and microscopic structure as well as as the emission, excitation and thermoluminescence properties of the non-doped, Eu^{2+} doped and Eu^{2+},Dy^{3+} co-doped distrontium magnesium disilicates ($Sr_2MgSi_2O_7$:Eu^{2+},Dy^{3+}) were studied using the XPD, TEM, TL and SR luminescence spectroscopy methods. The density functional theory calculations were used to study the total energy, structural modifications, host band structure, band gap energy as well as defect energies in the $Sr_2MgSi_2O_7$ and $SrAl_2O_4$ hosts.

The XPD patterns of the $Sr_2MgSi_2O_7$:Eu^{2+}(,Dy^{3+}) materials prepared with solid state reactions indicated that the introduction of the Eu^{2+} and Dy^{3+} ions favor the formation of the desired tetragonal $Sr_2MgSi_2O_7$ phase. $Sr_3MgSi_2O_8$ was also observed as a minor impurity phase.

Modification of the local structure due to the lattice defects was found using high-resolution TEM. Undisturbed crystal planes were frequently observed in the non-doped $Sr_2MgSi_2O_7$, whilst significant discontinuities were more frequently observed for the Eu^{2+} doped and especially the Eu^{2+},Dy^{3+} co-doped materials. The lattice domains seem to be created by point defects such as Dy^{3+} and cation vacancies which cause discontinuities in the crystal structure. Increased disorder is thus mainly due to the charge compensation effects.

The differences in the total energies show that the formation of the oxygen vacancy is more feasible than the creation of the strontium vacancy. The structural modifications in $Sr_2MgSi_2O_7$ and $SrAl_2O_4$ were slightly more pronounced around the Eu^{2+} centre than in the environment of Sr^{2+}. The structural effects induced by the strontium vacancy are more profound than the effect of the other vacancies and Eu^{2+}.

The band gap energy provides the basic data for the determination of the electronic structure. The calculated band gaps of $Sr_2MgSi_2O_7$ and $SrAl_2O_4$ agree very well with the ones derived from the synchrotron radiation excitation spectra. The valence band of both materials has mainly oxygen character, whereas the bottom of the conduction band consists mostly of the strontium states. This suggests that the oxygen vacancies do not have a significant effect on the conduction band or on the band gap energy, whereas the strontium vacancy increases the band gap.

The Eu^{2+} $4f^7$ ground state energy determines if blue light can be used in addition to UV to produce persistent luminescence. This state was located in the energy gap and linearly closer to the valence band for the higher Hubbard parameter U values. A careful comparison between the experimental and calculated results is necessary to determine the U value since its reliable calculation in these hosts does not seem possible.

The calculations show also that the energy difference between the two luminescence bands observed from $SrAl_2O_4$:Eu^{2+} at low temperatures may be explained by luminescence originating rather from a higher excited Eu^{2+} $4f^6 5d^1$ state than from the two crystallographic Sr sites.

Both positive and negative effect of the R^{3+} co-doping for the persistent luminescence has been found, though their origin has remained largely unknown. The $R^{2+/3+}$ $4f^n$ and $4f^{n-1} 5d^1$ ground states in the $Sr_2MgSi_2O_7$ band structure were calculated using *ab initio* methods for the first time. A good agreement between the calculations and the empirical model was found for the trends and energies of the R^{3+} $4f^n$ and $R^{2+/3+}$ $4f^{n-1} 5d^1$ ground states. However, the description of the R^{2+} $4f^n$ ground state energies was significantly less successful.

The determination of the defect and dopant energies in the host is a long-standing problem since they are extremely difficult to study experimentally. The calculated results suggest that even without the introduction of defects in the material, an intrinsic electron trap exists in the non-doped $SrAl_2O_4$ and possibly also in $Sr_2MgSi_2O_7$. The Eu^{2+} centre and the R^{3+} ions create electron traps in addition to the strontium and especially the oxygen vacancies in $Sr_2MgSi_2O_7$ and $SrAl_2O_4$. These trap energies are in a suitable range to be bleached by the thermal energy at room temperature. The oxygen vacancies form also very shallow electron traps which can decrease the duration of persistent luminescence since they are quickly bleached.

Very deep electron traps which are not expected to be involved in the persistent luminescence (but potentially in OSL) were created by the oxygen and aluminium vacancies. Strontium, magnesium, silicon and aluminium vacancies create also very shallow hole traps in $Sr_2MgSi_2O_7$ and $SrAl_2O_4$. The role of such traps in the persistent luminescence of the Eu^{2+} doped materials is probably not significant.

The interactions within the defect aggregates were found to modify clearly the traps created by both the Eu^{2+} centre and the vacancies. The modifications induced by the defect aggregation may

play a very significant role in the total trap structure since the total number of defects and dopants is expected to be high.

The calculated trap energy range is in agreement with the experimental trap structure of the $Sr_2MgSi_2O_7$:Eu^{2+}(,R^{3+}) materials obtained using thermoluminescence. The shallowest calculated traps cannot be compared with the experimental data since they have to be probed using low temperature TL measurements. The differences between the calculated and experimental trap structures are probably partly due to the modification of the traps by the Eu^{2+} and/or R^{3+} ions. A perfect agreement with the two trap structures is probably impossible to reach due to the simultaneous presence of multiple defect types in the host as well as complex interactions between them.

The combined thermoluminescence, photoluminescence and DFT results suggest that the deepening of the electron traps due to the Eu^{2+},R^{3+} co-doping combined with the increased number of the electron traps results in the efficient energy storage and very long duration and enhanced intensity of persistent luminescence from selected $Sr_2MgSi_2O_7$:Eu^{2+},R^{3+} materials. These results suggest that the intrinsic and defect based electron traps act together as energy storage sites. The trap depths have yet to be carefully determined since they have a significant effect on the persistent luminescence efficiency because this process is controlled by minute amounts of thermal energy.

The DFT calculations are an invaluable asset for the accurate simulation of defects in the solid state materials. Further studies using even larger superlattices are still needed to explore the modifications in the crystal and electronic host band structure induced by defect aggregates consisting of multiple defects. These include the Eu^{2+} luminescent centre, $R^{2+/3+}$ co-dopants and vacancies as well as interstitial ions. The use of larger lattices will enable a more versatile tailoring of the distances between the defects while it is unfortunately limited by the increased computational effort. The DFT method can be applied to other rare earth doped materials as well; however, the hosts with increasing lattice covalency may be described less accurately than the more ionic ones. A more reliable comparison between the calculated and experimental trap structure would also be facilitated by a careful optimization of the materials preparation conditions first to obtain single phase materials and second to favor the formation of different defect species.

REFERENCES

1. Williams, F., *Theoretical Basis for Solid-State Luminescence*, In: Goldberg, P. (Ed.), *Luminescence of Inorganic Solids*, Academic Press, New York, USA, 1966, p. 2.

2. Kano, T., *Luminescence Centres of Rare-Earth Ions*, In: Shionoya, S. and Yen, W.M. (Eds.), *Phosphor Handbook*, CRC Press, Boca Raton, FL, USA, 1999, pp. 178-200.

3. Aitasalo, T., Dereń, P., Hölsä, J., Jungner, H., Krupa, J.-C., Lastusaari, M., Legendziewicz, J., Niittykoski, J., and Stręk, W., *J. Solid State Chem.* **171** (2003) 114.

4. Halperin, A., *Activated Thermoluminescence (TL) Dosimeters and Related Radiation Detectors*, In: Gschneidner, K.A. Jr. and Eyring L., (Eds.), *Handbook Phys. Chem. Rare Earths*, vol. 28, Elsevier, Amsterdam, The Netherlands, 2000, pp. 274-275.

5. de Chermont, Q.L., Chanéac, C., Seguin, J., Pellé, F., Maîtrejean, S., Jolivet, J.-P., Gourier, D., Bessodes, M., and Scherman, D., *Proc. Natl. Acad. Sci. USA* **104** (2007) 9266.

6. Yamamoto, H. and Matsuzawa, T., *J. Lumin.* **72-74** (1997) 287.

7. Nakazawa, E. and Mochida, T., *J. Lumin.* **72-74** (1997) 236.

8. Matsuzawa, T., Aoki, Y., Takeuchi N., and Murayama, Y., *J. Electrochem. Soc.* **143** (1996) 2670.

9. Lin, Y., Tang, Z., Zhang, Z., and Nan, C.W., *Appl. Phys. Lett.* **81** (2002) 996.

10. Chen, Y., Liu, B., Kirm, M., Qi, Z., Shi, C., True, M., Vielhauer, S., and Zimmerer, G., *J. Lumin.* **118** (2006) 70.

11. Lin, Y., Nan, C.-W., Zhou, X., Wu, J., Wang, H., Chen, D., and Xu, S., *Mater. Chem. Phys.* **82** (2003) 860.

12. Lin, Y., Tang, Z., Zhang, Z., Wang, X., and Zhang, J., *J. Mater. Sci. Lett.* **20** (2001) 1505.

13. Setlur, A.A., Srivastava, A.M., Pham, H.L., Hannah, M.E., and Happek, U., *J. Appl. Phys.* **103** (2008) 053513.

14. Aitasalo, T., Hölsä, J., Jungner, H., Lastusaari, M., and Niittykoski, J., *J. Phys. Chem. B* **110** (2006) 4589.

15. Dorenbos, P., *J. Phys.: Condens. Matter* **15** (2003) 8417.

16. Dorenbos, P., *Phys. Stat. Sol. b* **242** (2005) R7.

17. Hölsä, J., Niittykoski, J., Kirm, M., Laamanen, T., Lastusaari, M., Novák, P., and Raud, J., *ECS Trans.* **6** (2008) 1.

18. Born, M. and Oppenheimer, R., *Ann. Phys. Leipzig* **84** (1927) 457.

19. Slater, J.C., *Rev. Mod. Phys.* **35** (1963) 484.

20. Slater, J.C., *Phys. Rev.* **35** (1930) 509.

21. Fock, V., *Z. Phys.* **61** (1930) 126.

22. Hohenberg, P. and Kohn, W., *Phys. Rev.* **136** (1964) B864.

23. Dreizler, R.M. and Gross, E.K.U., *Density Functional Theory: an Approach to the Quantum Many-Body Problem*, Springer, Berlin, Germany, 1990, pp. 4-10.

24. Singh, D.J., *Planewaves, Pseudopotentials and the* LAPW *Method*, Kluwer, Norwell, MA, USA, 1994, pp. 5-9.

25. Perdew, J.P., Chevary, J.A., Vosko, S.H., Jackson, K.A., Pederson, M.R., Singh, D.J., and Fiolhais, C., *Phys. Rev. B* **46** (1992) 6671.

26. Perdew, J.P. and Wang, Y., *Phys. Rev. B* **45** (1992) 13244.

27. Becke, A.D., *Phys. Rev. A* **38** (1988) 3098.

28. Langreth, D.C. and Mehl, M.J., *Phys. Rev. B* **28** (1983) 1809.

29. Novák, P., Kunes, J., Chaput, L., and Pickett, W.E., *Phys. Stat. Sol. b* **243** (2006) 563.

30. Becke, A.D., *J. Chem. Phys.* **98** (1993) 5648.

31. Stephens, P.J., Devlin, F.J., Chabalowski, C.F., and Frisch, M.J., *J. Phys. Chem.* **98** (1994) 11623.

32. de Pinho Ribeiro Moreira, I., Illas, F., and Martin, R.L., *Phys. Rev. B* **65** (2002) 155102.

33. Kohn, W. and Sham, L.J., *Phys. Rev.* **140** (1965) A1133.

34. Sushko, P.V., Shluger, A.L., and Catlow, C.R.A., *Surf. Sci.* **450** (2000) 153.

35. Dick, B.G. and Overhauser, A.W., *Phys. Rev.* **112** (1958) 90.

36. Cottenier, S., *Density Functional Theory and the Family of (L)APW-Methods: a Step-by-Step Introduction*, Instituut voor Kern- en Stralingsfysica, K.U. Leuven, Belgium, 2002, p. 6.

37. Slater, J.C., *Adv. Quantum Chem.* **1** (1964) 35.

38. Slater, J.C., *Phys. Rev.* **51** (1937) 846.

39. Zhang, H. and Wu, H., *Phys. Stat. Sol. b* **245** (2008) 37.

40. Peng, F., Chen, D., Fu, H., and Cheng, X., *Physica B* **403** (2008) 4259.

41. Xiao, B., Feng, J., Zhou, C.T., Xing, J.D., Xie, X.J., Cheng, Y.H., and Zhou, R., *Physica B* **405** (2010) 1274.

42. Dudarev, S.L., Botton, G.A., Savrasov, S.Y., Humphreys, C.J., and Sutton, A.P., *Phys. Rev. B* **57** (1998) 1505.

43. Tuncel, E., Colakoglu, K., Deligoz, E., and Ciftci, Y.O., *J. Phys. Chem. Solids* **70** (2009) 371.

44. Díaz-Sánchez, L.E., Romero, A.H., Cardona, M., Kremer, R.K., and Gonze, X., *Phys. Rev. Lett.* **99** (2007) 165504.

45. Baroni, S., de Gironcoli, S., Dal Corso, A., and Giannozzi, P., *Rev. Mod. Phys.* **73** (2001) 515.

46. Refson, K., Tulip, P.R., and Clark, S.J., *Phys. Rev. B* **73** (2006) 155114.

47. Adams, M.A., Refson, K., and Gabrys, B.J., *Phys. Chem. Chem. Phys.* **7** (2005) 3685.

48. Díaz-Sánchez, L.E., Romero, A.H., and Gonze, X., *Phys. Rev. B* **76** (2007) 104302.

49. Verstraete, M.J. and Gonze, X., *Phys. Rev. B* **74** (2006) 153408.

50. Caracas, R. and Gonze, X., *Phys. Rev. B* **68** (2003) 184102.

51. Caracas, R. and Gonze, X., *Phys. Rev. B* **71** (2005) 054101.

52. Du, J. and Corrales, R., *J. Phys. Chem. B* **110** (2006) 22346.

53. Schmidt, M., Ratcliff, W., Radaelli, P.G., Refson, K., Harrison, N.M., and Cheong, S.W., *Phys. Rev. Lett.* **92** (2004) 056402.

54. Anisimov, V.I., Solovyev, I.V., Korotin, M.A., Czyzyk, M.T., and Sawatzky, G.A., *Phys. Rev. B* **48** (1993) 16929.

55. Fu, Z., Zhou, S., Pan, T., and Zhang, S., *J. Solid State Chem.* **178** (2005) 230.

56. Rignanese, G.-M., Detraux, F., Gonze, X., Bongiorno, A., and Pasquarello, A., *Phys. Rev. Lett.* **89** (2002) 117601.

57. Detraux, F., Finocchi, F., and Gonze, X., *Phys. Rev. B* **73** (2006) 165208.

58. Novák, P. and Knízek, K., *J. Magn. Magn. Mater.* **316** (2007) e587.

59. Novák, P. and Rusz, J., *Phys. Rev. B* **71** (2005) 184433.

60. Pask, J.E., Singh, D.J., Mazin, I.I., Hellberg, C.S., and Kortus, J., *Phys. Rev. B* **64** (2001) 024403.

61. Tran, F., Blaha, P., Schwarz, K., and Novák, P., *Phys. Rev. B* **74** (2006) 155108.

62. Madsen, G.K.H. and Novák, P., *Europhys. Lett.* **69** (2005) 777.

63. Torumba, D., Novák, P., and Cottenier, S., *Phys. Rev. B* **77** (2008) 155101.

64. Novák, P., Kunes, J., Pickett, W.E., Ku, W., and Wagner, F.R., *Phys. Rev. B* **67** (2003) 140403.

65. Novák, P. and Wagner, F., *Phys. Rev. B* **66** (2002) 184434.

66. Kunes, J., Novák, P., Oppeneer, P.M., König, C., Fraune, M., Rüdiger, U., Güntherodt, G., and Ambrosch-Draxl, C., *Phys. Rev. B* **65** (2002) 165105.

67. Novák, P., Kunes, J., and Oppeneer, P.M., *Physica B* **312-313** (2002) 785.

68. Kunes, J. and Novák, P., *J. Phys.: Condens. Matter.* **11** (1999) 6301.

69. Sawada, H., Morikawa, Y., Terakura, K., and Hamada, N., *Phys. Rev. B* **56** (1997) 12154.

70. Goubin, F., Rocquefelte, X., Pauwels, D., Tressaud, A., Demourgues, A., Jobic, S., and Montardi, Y., *J. Solid State Chem.* **177** (2004) 2833.

71. Chong, D.P., Segala, M., Takahata, Y., and Baerends, E.J., *Int. J. Quantum Chem.* **108** (2008) 1358.

72. Görling, A., Heinze, H.H., Ruzankin, S.P., Staufer, M., and Rösch, N., *J. Chem. Phys.* **110** (1999) 2785.

73. Stratmann, R.E., Scuseria, G.E., and Frisch, M.J., *J. Chem. Phys.* **109** (1998) 8218.

74. Markovits, A., Minot, C., Ménétrey, M., Sousa, C., and Illas, F., *Solid State Ionics* **178** (2007) 173.

75. Henriques, J.M., Caetano, E.W.S., Freire, V.N., da Costa, J.A.P., and Albuquerque, E.L., *J. Solid State Chem.* **180** (2007) 974.

76. Wang, Y., Zhang, Z., Zhang, J., and Lu, Y., *J. Solid State Chem.* **182** (2009) 813.

77. Barboza, C.A., Henriques, J.M., Albuquerque, E.L., Freire, V.N., da Costa, J.A.P., and Caetano, E.W.S., *J. Phys. D: Appl. Phys.* **42** (2009) 155406.

78. Walsh, A., Yan, Y., Huda, M.N., Al-Jassim, M.M., and Wei, S.-H., *Chem. Mater.* **21** (2009) 547.

79. Gougoussis, C., Calandra, M., Seitsonen, A.P., and Mauri, F., *Phys. Rev. B* **80** (2009) 075102.

80. Novák, P., Boucher, F., Gressier, P., Blaha, P., and Schwarz, K., *Phys. Rev. B* **63** (2001) 235114.

81. Carrasco, J., Lopez, N., Sousa, C., and Illas, F., *Phys. Rev. B* **72** (2005) 054109.

82. Avdeev, V.I. and Zhidomirov, G.M., *J. Struct. Chem.* **44** (2003) 918. Translated from *Zh. Strukt. Khim.* **44** (2003) 995.

83. Brazzelli, S., Di Valentin, C., Pacchioni, G., Giamello, E., and Chiesa, M., *J. Phys. Chem. B* **107** (2003) 8498.

84. Di Valentin, C., Ricci, D., Pacchioni, G., Chiesa, M., Paganini, M.C., and Giamello, E., *Surf. Sci.* **521** (2002) 104.

85. Raghavachari, K., Ricci, D., and Pacchioni, G., *J. Chem. Phys.* **116** (2002) 825.

86. Liu, W. and Dolg, M., *Phys. Rev. A* **57** (1998) 1721.

87. Adamo, C. and Maldivi, P., *J. Phys. Chem. A* **102** (1998) 6812.

88. Luo, Y., Wan, X., Ito, Y., Takami, S., Kubo, M., and Miyamoto, A., *Chem. Phys.* **282** (2002) 197.

89. Wang, S.G., Pan, D.K., and Schwarz, W.H.E., *J. Chem. Phys.* **102** (1995) 9296.

90. Heiberg, H., Gropen, O., Laerdahl, J.K., Swang, O., and Wahlgren, U., *Theor. Chem. Acc.* **110** (2003) 118.

91. Kunes, J. and Pickett, W.E., *Physica B* **359-361** (2005) 205.

92. Yang, J. and Dolg, M., *Theor. Chem. Acc.* **113** (2005) 212.

93. Yakovkin, I.N., *Appl. Surf. Sci.* **256** (2010) 4845.

94. Zhu, J., Cheng, W.-D., Zhang, H., and Wang, Y.-D., *J. Lumin.* **129** (2009) 1326.

95. Zhu, J., Cheng, W.-D., Wu, D.-S., Zhang, H., Gong, Y.-J., Tong, H.-N., and Zhao, D., *J. Alloys Compd.* **454** (2008) 419.

96. Larson, P., Lambrecht, W.R.L., Chantis, A., and van Schilfgaarde, M., *Phys. Rev. B* **75** (2007) 045114.

97. Novák, P. and Divis, M., *Phys. Stat. Sol. b* **244** (2007) 3168.

98. Llanos, J., Conejeros, S., Cortés, R., Sánchez, V., Barahona, P., and Pena, O., *Mater. Res. Bull.* **43** (2008) 312.

99. Klier, K., Novák, P., Miller, A.C., Spirko, J.A., and Hatalis, M.K., *J. Phys. Chem. Solids* **70** (2009) 1302.

100. Klintenberg, M., Weber, M.J., Dujardin, C., Eriksson, O., and Derenzo, S.E., *Radiat. Eff. Defects Solids* **154** (2001) 231.

101. Said, M., Ben Zik, F., Bertoni, C.M., and Ossicini, S., *Eur. Phys. J. B* **23** (2001) 191.

102. Zhong, G., Lei, X., and Mao, J., *Phys. Rev. B* **79** (2009) 094424.

103. Hermes, W., Al Alam, A.F., Matar, S.F., and Pöttgen, R., *Solid State Sci.* **10** (2008) 1895.

104. Janatová, M., Poltierová Vejpravová, J., and Divis, M., *J. Magn. Magn. Mater.* **322** (2010) 1140.

105. Lincke, H., Glaum, R., Dittrich, V., Tegel, M., Johrendt, D., Hermes, W., Möller, M.H., Nilges, T., and Pöttgen, R., *Z. Anorg. Allg. Chem.* **634** (2008) 1339.

106. Petit, S., Jones, R., Shaw, M.J., Briddon, P.R., Hourahine, B., and Frauenheim, T., *Phys. Rev. B* **72** (2005) 073205.

107. Jones, R., *Opt. Mater.* **28** (2006) 718.

108. Prezzi, D., Eberlein, T.A.G., Jones, R., Filhol, J.-S., Coutinho, J., Shaw, M.J., and Briddon, P.R., *Phys. Rev. B* **71** (2005) 245203.

109. Prezzi, D., Eberlein, T.A.G., Filhol, J.-S., Jones, R., Shaw, M.J., Briddon, P.R., and Öberg, S., *Phys. Rev. B* **69** (2004) 193202.

110. Brik, M.G., Sildos, I., and Kiisk, V., *Physica B* **405** (2010) 2450.

111. Sanna, S., Schmidt, W.G., Frauenheim, T., and Gerstmann, U., *Phys. Rev. B* **80** (2009) 104120.

112. Sanna, S., Frauenheim, T., and Gerstmann, U., *Phys. Rev. B* **78** (2008) 085201.

113. Filhol, J.-S., Jones, R., Shaw, M.J., and Briddon, P.R., *Appl. Phys. Lett.* **84** (2004) 2841.

114. Coutinho, J., Jones, R., Shaw, M.J., Briddon, P.R., and Öberg, S., *Appl. Phys. Lett.* **84** (2004) 1683.

115. Clabau, F., Rocquefelte, X., Jobic, S., Deniard, P., Whangbo, M.-H., Garcia, A., and Le Mercier, T., *Chem. Mater.* **17** (2005) 3904.

116. Zhukovskii, Y.F., Pugno, N., Popov, A.I., Balasubramanian, C., and Bellucci, S., *J. Phys.: Condens. Matter* **19** (2007) 395021.

117. Jeong, J.-W. and Oshiyama, A., *Phys. Rev. B* **64** (2001) 235204.

118. Pacchioni, G., Erbetta, D., Ricci, D., and Fanciulli, M., *J. Phys. Chem. B* **105** (2001) 6097.

119. Yin, X., Stott, M.J., and Rubio, A., *Phys. Rev. B* **68** (2003) 205205.

120. Astala, R., Calderín, L., Yin, X., and Stott, M.J., *Chem. Mater.* **18** (2006) 413.

121. Justicia, I., Ordejón, P., Canto, G., Mozos, J.L., Fraxedas, J., Battiston, G.A., Gerbasi, R., and Figueras, A., *Adv. Mater.* **14** (2002) 1399.

122. Cuong, D.D., Lee, B., Choi, K.M., Ahn, H.-S., Han, S., and Lee, J., *Phys. Rev. Lett.* **98** (2007) 115503.

123. Evarestov, R.A., Kotomin, E.A., and Zhukovskii, Y.F., *Int. J. Quantum Chem.* **106** (2006) 2173.

124. Astala, R. and Bristowe, P.D., *Comp. Mater. Sci.* **22** (2001) 81.

125. Predith, A., Ceder, G., Wolverton, C., Persson, K., and Mueller, T., *Phys. Rev. B* **77** (2008) 144104.

126. Pornprasertsuk, R., Ramanarayanan, P., Musgrave, C.B., and Prinz, F.B., *J. Appl. Phys.* **98** (2005) 103513.

127. Foster, A.S., Sulimov, V.B., Lopez Gejo, F., Shluger, A.L., and Nieminen, R.M., *Phys. Rev. B* **64** (2001) 224108.

128. Ferro, R., Rodríguez, J.A., Verstraete, M., Solomko, V., and Bertrand, P., *Phys. Stat. Sol. c* **2** (2005) 3548.

129. Shi, H., Jia, R., and Eglitis, R.I., *Phys. Rev. B* **81** (2010) 195101.

130. Foster, A.S., Lopez Gejo, F., Shluger, A.L., and Nieminen, R.M., *Phys. Rev. B* **65** (2002) 174117.

131. Evarestov, R.A., *Phys. Stat. Sol. a* **2** (2005) 235.

132. Alfredsson, M., Brodholt, J.P., Dobson, D.P., Oganov, A.R., Catlow, C.R.A., Parker, S.C., and Price, G.D., *Phys. Chem. Miner.* **31** (2005) 671.

133. Rignanese, G.-M., De Vita, A., Charlier, J.-C., Gonze, X., and Car, R., *Phys. Rev. B* **61** (2000) 13250.

134. Fox, H., Horsfield, A.P., and Gillan, J., *J. Chem. Phys.* **124** (2006) 134709.

135. Hejduk, P., Witko, M., and Hermann, K., *Top. Catal.* **52** (2009) 1105.

136. Piskunov, S., Kotomin, E.A., and Heifets, E., *Microelectron. Eng.* **81** (2005) 472.

137. Borstel, G., Eglitis, R.I, Kotomin, E.A., and Heifets, E., *J. Cryst. Growth* **237-239** (2002) 687.

138. Verstraete, M.J., Dumont, J., Sporken, R., Johnson, R.L., Wiame, F., Temst, K., Swerts, J., Mirabella, F., Ghijsen, J., and Gonze, X., *Phys. Rev. B* **70** (2004) 205427.

139. Kökten, H. and Erkoc, S., *Int. J. Modern Phys. C* **17** (2006) 795.

140. Licona, R. and Rivas-Silva, J.F., *Int. J. Quantum Chem.* **104** (2005) 919.

141. Pacchioni, G., *Solid State Sci.* **2** (2000) 161.

142. Watson, G.W., *Radiat. Eff. Defects Solids* **157** (2002) 773.

143. Scanlon, D.O., Walsh, A., Morgan, B.J., Nolan, M., Fearon, J., and Watson, G.W., *J. Phys. Chem. C* **111** (2007) 7971.

144. Morgan, B.J. and Watson, G.W., *Surf. Sci.* **601** (2007) 5034.

145. Ferrari, A.M., Pisani, C., Cinquini, F., Giordano, L., and Pacchioni, G., *J. Chem. Phys.* **127** (2007) 174711.

146. Prades, J.D., Cirera, A., Morante, J.R., and Cornet, A., *Thin Solid Films* **515** (2007) 8670.

147. Carrasco, J., Illas, F., Lopez, N., Kotomin, E.A., Zhukovskii, Y.F., Evarestov, R.A., Mastrikov, Y.A., Piskunov, S., and Maier, J., *Phys. Rev. B* **73** (2006) 064106.

148. Yang, Z., Yu, X., Lu, Z., Li, S., and Hermansson, K., *Phys. Lett. A* **373** (2009) 2786.

149. Nolan, M., Fearon, J.E., and Watson, G.W., *Solid State Ionics* **177** (2006) 3069.

150. Nolan, M., Parker, S.C., and Watson, G.W., *Surf. Sci.* **595** (2005) 223.

151. Del Vitto, A., Pacchioni, G., Delbecq, F., and Sautet, P., *J. Phys. Chem. B* **109** (2005) 8040.

152. Zaitsev, A.L., Detraux, F., Pleskachevskii, Y.M., and Gonze, X., *Phys. Solid State* **45** (2003) 2218. Translated from *Fiz. Tverd. Tela* **45** (2003) 2118.

153. Dai, Y., Han, S., Dai, D., Zhang, Y., and Qi, Y., *Solid State Commun.* **126** (2003) 103.

154. Snijders, P.C., Moon, E.J., González, C., Rogge, S., Ortega, J., Flores, F., and Weitering, H.H., *Phys. Rev. Lett.* **99** (2007) 116102.

155. Snijders, P.C., Rogge, S., González, C., Pérez, R., Ortega, J., Flores, F., and Weitering, H.H., *Phys. Rev. B* **72** (2005) 125343.

156. Wiame, F., Dumont, J., Sporken, R., Verstraete, M., and Gonze, X., *Phys. Rev. B* **72** (2005) 033302.

157. Pfnür, H., Tegenkamp, C., Maslyuk, V., and Bredow, T., *Surf. Sci.* **600** (2006) 1664.

158. Wang, Y., Nguyen, H.N., and Truong, T.N., *Chem. Eur. J.* **12** (2006) 5859.

159. Di Valentin, C., Ferullo, R., Binda, R., and Pacchioni, G., *Surf. Sci.* **600** (2006) 1147.

160. Chiesa, M., Paganini, M.C. Spoto, G., Giamello, E., Di Valentin, C., Del Vitto, A., and Pacchioni, G., *J. Phys. Chem. B* **109** (2005) 7314.

161. Zhu, J., Farmer, J.A., Ruzycki, N., Xu, L., Campbell, C.T., and Henkelman, G., *J. Am. Chem. Soc.* **130** (2008) 2314.

162. Branda, M.M., Ferullo, R.M., Belelli, P.G., and Castellani, N.J., *Surf. Sci.* **527** (2003) 89.

163. Rodriguez, J.A. and Maiti, A., *J. Phys. Chem. B* **104** (2000) 3630.

164. Nolan, M. and Watson, G.W., *Surf. Sci.* **586** (2005) 25.

165. Du, Z. and de Leeuw, N.H., *Surf. Sci.* **554** (2004) 193.

166. Martinez, U., Giordano, L., and Pacchioni, G., *J. Phys. Chem. B* **110** (2006) 17015.

167. Wendt, S., Schaub, R., Matthiesen, J., Vestergaard, E.K., Wahlström, E., Rasmussen, M.D., Thostrup, P., Molina, L.M., Laegsgaard, E., Stensgaard, I., Hammer, B., and Besenbacher, F., *Surf. Sci.* **598** (2005) 226.

168. Wang, Y. and Hwang, G.S., *Surf. Sci.* **542** (2003) 72.

169. Sorescu, D.C. and Yates, J.T., *J. Phys. Chem. B* **106** (2002) 6184.

170. Witko, M., Grybos, R., and Tokarz-Sobieraj, R., *Top. Catal.* **38** (2006) 105.

171. Haber, J. and Witko, M., *J. Catal.* **216** (2003) 416.

172. Hermann, K., Witko, M., Druzinic, R., and Tokarz, R., *Appl. Phys. A* **72** (2001) 429.

173. Liu, Z.-P. and Hu, P., *J. Am. Chem. Soc.* **125** (2003) 1958.

174. Nolan, M., Parker, S.C., and Watson, G.W., *J. Phys. Chem. B* **110** (2006) 2256.

175. Herschend, B., Baudin, M., and Hermansson, K., *Chem. Phys.* **328** (2006) 345.

176. Müller, C., Freysoldt, C., Baudin, M., and Hermansson, K., *Chem. Phys.* **318** (2005) 180.

177. Chung, K.S., *TL Glow Curve Analyzer v. 1.0.3*, Korea Atomic Energy Research Institute and Gyeongsang National University, Korea, 2008.

178. Chung, K.S., Choe, H.S., Lee, J.I., Kim, J.L., and Chang, S.Y., *Radiat. Prot. Dosim.* **115** (2005) 345.

179. http://hasylab.desy.de/facilities/doris_iii/beamlines/i_superlumi

180. Poort, S.H.M., Blokpoel, W.P., and Blasse, G., *Chem. Mater.* **7** (1995) 1547.

181. Blaha, P., Schwarz, K., Madsen, G.K.H., Kvasnicka, D., and Luitz, J., In: Schwarz, K. (Ed.), WIEN2k, *An Augmented Plane Wave + Local Orbitals Program for Calculating Crystal Properties*, Vienna University of Technology, Vienna, Austria, 2001.

182. Liechtenstein, A.I., Anisimov, V.I., and Zaanen, J., *Phys. Rev. B* **52** (1995) R5467.

183. Anisimov, V.I., Aryasetiawan, F., and Lichtenstein, A.I., *J. Phys.: Condens. Matter* **9** (1997) 767.

184. Solovyev, I.V., Dederichs, P.H., and Anisimov, V.I., *Phys. Rev. B* **50** (1994) 16861.

185. Richter, M., Oppeneer, P.M., Eschrig, H., and Johansson, B., *Phys. Rev. B* **46** (1992) 13919.

186. Brooks, M.S.S., Nordström, L., and Johansson, B., *Physica B* **172** (1991) 95.

187. Richter, M. and Eschrig, H., *Physica B* **172** (1991) 85.

188. Kimata, M., *Z. Kristallogr.* **163** (1983) 295.

189. Schulze, A.R. and Müller-Buschbaum, H.K., *Z. Anorg. Allg. Chem.* **475** (1981) 205.

190. Kraus, W. and Nolze, G., *POWDERCELL for Windows, v. 2.4*, Federal Institute for Materials Research, Berlin, Germany, 2000.

191. Shannon, R.D., *Acta Cryst. A* **32** (1976) 751.

192. Qi, Z., Shi, C., Liu, M., Zhou, D., Luo, X., Zhang, J., and Xie, Y., *Phys. Stat. Sol. a* **201** (2004) 3109.

193. Aitasalo, T., Hölsä, J., Jungner, H., Krupa, J.-C., Lastusaari, M., Legendziewicz, J., and Niittykoski, J., *Radiat. Meas.* **38** (2004) 727.

194. Aitasalo, T., Hassinen, J., Hölsä, J., Laamanen, T., Lastusaari, M., Malkamäki, M., Niittykoski, J., and Novák, P., *J. Rare Earths* **27** (2009) 529.

195. Blasse, G., Wanmaker, W.L., ter Vrugt, J.W., and Bril, A., *Philips Res. Rep.* **23** (1968) 189.

196. Grimm, J., Suyver, J.F., Beurer, E., Carver, G., and Güdel, H.U., *J. Phys. Chem. B* **110** (2006) 2093.

197. Grimm, J. and Güdel, H.U., *Chem. Phys. Lett.* **404** (2005) 40.

198. Hölsä, J., Lastusaari, M., Maryško, M., and Tukia M., *J. Solid State Chem.* **178** (2005) 435.

199. Dorenbos, P., *J. Phys.: Condens. Matter* **15** (2003) 575.

200. Jörgensen, C.K., *Mol. Phys.* **5** (1962) 271.

201. Dorenbos, P., *J. Electrochem. Soc.* **152** (2005) H107.

202. Hölsä, J., Kotlov, A., Laamanen, T., Lastusaari, M., Malkamäki, M., and Novák, P., in preparation.

203. Sabbagh Alvani, A.A., Moztarzadeh, F., and Sarabi, A.A., *J. Lumin.* **114** (2005) 131.

204. van Haecke, J.E., Smet, P.F., and Poelman, D., *J. Lumin.* **126** (2007) 508.

205. Hölsä, J., Aitasalo, T., Jungner, H., Lastusaari, M., and Niittykoski, J., *J. Alloys Compd.* **374** (2004) 56.